Target-oriented wave-equation least-squares migration/inversion with phase-encoded Hessian

Yaxun Tang*

**Stanford Exploration Project, Geophysics Department, Stanford University, Stanford, CA 94305. E-mail: tang@sep.stanford.edu*

Presented at the 78th Annual Meeting, Society of Exploration Geophysicists, November 2008.

Manuscript submitted on 12/24/2008. Revised manuscript submitted on 4/29/2009.

(June 10, 2009)

GEO-2008-0443

Running head: **Inversion with phase-encoded Hessian**

ABSTRACT

Prestack depth migration produces blurred images due to limited acquisition apertures, complexities in the velocity model and bandlimited characteristics of seismic waves. This distortion can be partially corrected using the model-space least-squares migration/inversion approach, where a target-oriented wave-equation Hessian operator is first explicitly computed, and then inverse filtering is iteratively applied to deblur or invert for the reflectivity. However, one difficulty is the cost for computing the explicit Hessian operator, which requires storing a large number of Green's functions, making it challenging for large-scale applications. As a remedy to this difficulty, I present a new method for computing the Hessian operator for the wave-equation-based least-squares migration/inversion problem. The proposed method modifies the original explicit Hessian formula, enabling efficient com-

putation of this operator. A particular advantage of this method is that it eliminates on-disk storage of Green's functions. The modifications, however, also introduce undesired crosstalk artifacts. I examine two different phase-encoding schemes, namely, plane-wave-phase encoding and random-phase encoding, to suppress the crosstalk. I apply the randomly phase-encoded Hessian operator to the Sigsbee2A synthetic data set, where an improved subsalt image with more balanced amplitudes is obtained.

INTRODUCTION

Migration is an important tool for imaging subsurface structures using reflection seismic data. The classic imaging principle for shot-based migration states that reflectors are located where the forward-propagated source wavefield correlates with the backward-propagated receiver wavefield (Claerbout, 1971). However, this imaging principle is only the adjoint of the forward Born-modeling operator (Lailly, 1983), which provides reliable structural information of the subsurface, but blurs the image because of the non-unitary nature of the Born modeling operator. To deblur the migrated image and correct the effects of limited acquisition geometry, complex overburden and bandlimited wavefields, the imaging problem can be posed as an inverse problem based on the minimization of a least-squares functional. The inverse problem can be formulated either in the data space (Lailly, 1983; Tarantola, 1984; Nemeth, 1999; Kuhl and Sacchi, 2003; Clapp, 2005) or in the model space (Beylkin, 1985; Chavent and Plessix, 1999; Rickett, 2003; Sjoeberg et al., 2003; Guitton, 2004; Plessix and Mulder, 2004; Valenciano et al., 2006; Yu et al., 2006; Symes, 2008). The data-space approach can be solved iteratively using the gradient-based method (Nemeth, 1999; Kuhl and Sacchi, 2003; Clapp, 2005) without explicit construction of the Hessian, the matrix of the second derivatives of the error functional with respect to the model parameters. The iterative solving, however, is relatively costly and converges slowly without proper preconditioning.

On the other hand, the model-space approach requires explicitly constructing the Hessian and applying its pseudo-inverse to the migrated image. The full Hessian of the least-squares functional is too big and expensive to be computed in practical applications; hence some authors (Chavent and Plessix, 1999; Rickett, 2003; Plessix and Mulder, 2004; Symes,

2008) approximate it by a diagonal matrix. In the case of high-frequency asymptotics, and with an infinite aperture, the Hessian is diagonal in most cases (Beylkin, 1985). For a finite range of frequencies and limited acquisition geometry, however, the Hessian is no longer diagonal and not even diagonally dominant (Pratt et al., 1998; Chavent and Plessix, 1999; Plessix and Mulder, 2004; Valenciano et al., 2006). It has been shown by Albertin et al. (2004) and Valenciano (2008) that, in areas of poor illumination, e.g., subsalt regions, the Hessian's main diagonal energy is smeared along its off-diagonals. Therefore, a diagonal matrix has limited effect in deblurring the migrated image, especially in poorly illuminated areas. That is why several authors, e.g., Albertin et al. (2004) and Valenciano (2008), suggest computing a limited number of the Hessian off-diagonals to compensate for poor illumination and improve the inversion/deblurring result.

Since the exact Hessian off-diagonals are expensive to compute, some attempts have been made to reduce the cost by computing the non-diagonal Hessian in an approximate sense. Yu et al. (2006) introduce a lateral invariant non-diagonal Hessian by assuming a 1-D layered medium; Guitton (2004) uses a bank of non-stationary filters to approximate a non-diagonal inverse of the Hessian; with local plane-wave assumptions, Lecomte (1998), Gelius et al. (2002) and Lecomte (2008) compute the Hessian in the local phase domain using a ray-based approach. They demonstrate that, since ray tracing conveniently gives local propagation angles of both source and receiver rays, the local scattering wavenumber for image points in the subsurface can be efficiently constructed. However, the high-frequency asymptotic approximation and the caustics inherent in ray theory may prevent the ray-based approach accurately handle complex geologies (Hoffmann, 2001). To better honor the bandlimited nature of the seismic waves, Xie et al. (2006) use an one-way wave-equation-based approach to compute the phase-domain Hessian through local plane-wave decomposition. The above

theories of computing the local phase-domain Hessian operator assume the velocity model is locally homogeneous. Although this is a reasonable assumption for most cases, when there are sharp velocity contrasts as in the vicinities of salt boundaries, this assumption becomes less reliable.

Another way of computing the wave-equation non-stationary Hessian operator is through crosscorrelation of the source and receiver Green's functions in the space domain (Plessix and Mulder, 2004; Valenciano et al., 2006). This approach does not introduce any assumptions to the velocity model. However, computing even a limited number of the Hessian off-diagonals in the space domain, by directly implementing the explicit Hessian formula, is very cumbersome. A huge number of Green's functions (easily several hundred terabytes for a typical 3-D survey with a reasonable frequency band) must be pre-computed and stored and then read from the disk to generate the Hessian. Such operations not only require high-volume storage, but also high-speed I/O and network communication. Though computer speed continues to improve rapidly, computing the Hessian in such a way still presents a challenge.

To make the space-domain Hessian more affordable, I describe a method based on the phase-encoding technique. In this method, the original explicit Hessian formula is slightly modified to enable efficient computation of this operator. The proposed method makes the Hessian computation similar to the shot-profile migration, but with slightly modified imaging and boundary conditions for the wavefields. The new method eliminates the need to store Green's functions, but it also introduces crosstalk artifacts. I examine two phase-encoding schemes, plane-wave-phase encoding (Whitmore, 1995; Zhang et al., 2005; Liu et al., 2006) and random-phase encoding (Romero et al., 2000), to attenuate the crosstalk.

This paper is organized as follows. First, I briefly review the theory of formulating the inverse problem in the model space. Next, I discuss how the explicit Hessian can be efficiently computed using phase encoding. Finally, I apply the phase-encoded Hessian to deblur the migrated image for the Sigsbee2A model.

LEAST-SQUARES HESSIAN

Within limits of the Born approximation of the acoustic wave equation, the seismic data $d(\mathbf{x}_r, \mathbf{x}_s, \omega)$ recorded by a receiver at $\mathbf{x}_r = (x_r, y_r)$ due to a source at $\mathbf{x}_s = (x_s, y_s)$ can be modeled using a linear equation as follows (Stolt and Benson, 1986):

$$d(\mathbf{x}_r, \mathbf{x}_s, \omega) = \omega^2 \sum_{\mathbf{x}} f_s(\omega) G(\mathbf{x}, \mathbf{x}_s, \omega) G(\mathbf{x}, \mathbf{x}_r, \omega) m(\mathbf{x}), \tag{1}$$

where ω is the angular frequency; $f_s(\omega)$ is the source signature; and $m(\mathbf{x})$ denotes the reflectivity (a perturbed quantity from the background velocity) at image point $\mathbf{x} = (x, y, z)$ in the subsurface; $G(\mathbf{x}, \mathbf{x}_s, \omega)$ and $G(\mathbf{x}, \mathbf{x}_r, \omega)$ are the Green's functions connecting the source and receiver respectively, to the image point $\mathbf{x}$. Throughout this paper, we assume the Green's functions are computed by means of one-way wavefield extrapolation (Claerbout, 1985; Stoffa et al., 1990; Ristow and Rühl, 1994; Biondi, 2002). Although not discussed in this paper, Green's functions obtained using other methods, such as by solving two-way wave equation, can also be used under this framework.

In equation 1, we assume $\mathbf{x}_s$ and $\mathbf{x}_r$ are infinite in extent and independent of each other. For a real survey, however, we do not have infinitely long cable and infinitely many sources; thus we must introduce the following acquisition mask matrix to limit the size of

the modeling:

$$w(\mathbf{x}_r, \mathbf{x}_s) = \begin{cases} 1 & \text{if } \mathbf{x}_r \text{ is within the recording} \\ & \text{range of a shot at } \mathbf{x}_s; \\ 0 & \text{otherwise .} \end{cases} \tag{2}$$

In 2-D, for a marine acquisition geometry, $w(\mathbf{x}_r, \mathbf{x}_s)$ is similar to a band-limited diagonal matrix; for an Ocean Bottom Seismometer (OBS) or a land acquisition geometry, where all shots share the same receiver array, $w(\mathbf{x}_r, \mathbf{x}_s)$ is a rectangular matrix. In 3-D, the structure of the matrix is slightly more complicated.

To find a model that best fits the observed data, we can minimize the following objective function in the least-squares sense:

$$\begin{aligned} F &= \frac{1}{2} \sum_{\omega} \sum_{\mathbf{x}_s} \sum_{\mathbf{x}_r} |w(\mathbf{x}_r, \mathbf{x}_s) \\ &\quad \times [d(\mathbf{x}_r, \mathbf{x}_s, \omega) - d_{\text{obs}}(\mathbf{x}_r, \mathbf{x}_s, \omega)]|^2, \end{aligned} \tag{3}$$

where $d_{\text{obs}}(\mathbf{x}_r, \mathbf{x}_s, \omega)$ represents the observed data. It can be written in a more compact notation as follows:

$$F(\mathbf{m}) = \frac{1}{2} ||\mathbf{W}(\mathbf{d} - \mathbf{d}_{\text{obs}})||_2^2 = \frac{1}{2} ||\mathbf{W}(\mathbf{L}\mathbf{m} - \mathbf{d}_{\text{obs}})||_2^2, \tag{4}$$

where $\mathbf{L}$ is the forward modeling operator defined in equation 1, $\mathbf{W}$ is the acquisition mask operator described by equation 2, and $|| \cdot ||_2$ stands for the ℓ_2 norm. The data-space objective function $F(\mathbf{m})$ is usually minimized with a gradient-based optimization solver, which iterates until an acceptable image is obtained (Nemeth, 1999; Kuhl and Sacchi, 2003; Clapp, 2005). However, the data-space inversion scheme lacks flexibility and cannot be implemented in a target-oriented fashion. Full-domain migration/demigration has to be carried out within each iteration; and the optimization converges slowly without a proper

preconditioner. Therefore, the data-space inversion scheme is computationally challenging for large-scale applications.

Alternatively, we can reformulate the inverse problem and solve it in the model space. Because $\mathbf{L}$ is a linear operator, $F(\mathbf{m})$ is a quadratic function. $F(\mathbf{m})$ reaches its minimum when $\mathbf{m}$ satisfies (Tarantola, 1987):

$$\mathbf{m} = \mathbf{H}^{-1}\mathbf{L}^{*}\mathbf{W}^{*}\mathbf{d}_{\text{obs}}, \tag{5}$$

where * means adjoint (complex conjugation and transpose) and $\mathbf{H} = \mathbf{L}^{*}\mathbf{W}^{*}\mathbf{W}\mathbf{L}$ is the weighted Hessian operator. Equation 5 has only symbolic meaning, because the Hessian is often singular and its inverse is not easy to obtain directly. A more practical way would be reconstructing the reflectivity $\mathbf{m}$ through iterative inverse filtering by minimizing a model-space objective function defined as follows (Valenciano et al., 2006):

$$J(\mathbf{m}) = \frac{1}{2}||\mathbf{H}\mathbf{m} - \mathbf{m}_{\text{mig}}||_2^2, \tag{6}$$

where $\mathbf{m}_{\text{mig}} = \mathbf{L}^{*}\mathbf{W}^{*}\mathbf{d}_{\text{obs}}$ is the migrated image.

One advantage of the model-space formulation is that it can be implemented in a target-oriented fashion, which can substantially reduce the size of the problem and hence the computational cost (Valenciano et al., 2006; Valenciano, 2008). For example, we can choose to invert only areas of particular interest, such as subsalt regions, where potential reservoirs are located and migration often fails to provide reliable images. In fact, the model-space approach divides the inversion problem into two stages: computing the explicit Hessian (only once) and minimizing the objective function $J(\mathbf{m})$. Since the cost of minimizing the objective function $J(\mathbf{m})$ is relatively small once the explicit Hessian is obtained, various regularization schemes incorporating different *a priori* information can be easily tested at virtually little cost.

Each element of the Hessian is given as follows by taking the second derivative of the objective function $F(\mathbf{m})$ with respect to the model parameters (Plessix and Mulder, 2004; Valenciano et al., 2006); note that $w^2(\mathbf{x}_r, \mathbf{x}_s) = w^*(\mathbf{x}_r, \mathbf{x}_s) = w(\mathbf{x}_r, \mathbf{x}_s)$:

$$
\begin{aligned}
& H(\mathbf{x}, \mathbf{y}) \\
& = \Re \{ \sum_{\omega} \omega^4 \sum_{\mathbf{x}_s} |f_s(\omega)|^2 G(\mathbf{x}, \mathbf{x}_s, \omega) G^*(\mathbf{y}, \mathbf{x}_s, \omega) \\
& \times \sum_{\mathbf{x}_r} w(\mathbf{x}_r, \mathbf{x}_s) G(\mathbf{x}, \mathbf{x}_r, \omega) G^*(\mathbf{y}, \mathbf{x}_r, \omega) \} ,
\end{aligned} \tag{7}
$$

where $\Re$ denotes taking the real part of a complex value, and $\mathbf{y}$ is a neighbor point around the image point $\mathbf{x}$ in the subsurface. When $\mathbf{x} = \mathbf{y}$, we obtain the diagonal elements of the Hessian; when $\mathbf{x} \neq \mathbf{y}$, we obtain the off-diagonal elements. A target-oriented truncated Hessian is obtained by computing the Hessian for $\mathbf{x}$'s that are within the target zone and a small number of $\mathbf{y}$'s that are close to each $\mathbf{x}$ (Valenciano et al., 2006; Valenciano, 2008).

Hereafter, I call $H(\mathbf{x}, \mathbf{y})$ in equation 7 the exact Hessian, since it is derived strictly from the least-squares functional $F(\mathbf{m})$ in the shot-profile domain. However, direct implementation of equation 7 requires saving Green's functions, which may bring considerable computational issues, because the Green's functions can be huge for practical applications, especially in 3-D. To reduce the computational burden, in the subsequent sections, I introduce an alternative method based on phase encoding to compute the Hessian operator. As I will demonstrate, by using this approach, we do not need to save any Green's functions, and the cost is also significantly reduced.

PHASE-ENCODED HESSIAN

Encoding of the receiver-side Green's functions

Suppose we have a new operator $\widetilde{H}(\mathbf{x}, \mathbf{y}, \mathbf{p}_r)$ defined as follows:

$$\begin{aligned}
&\widetilde{H}(\mathbf{x}, \mathbf{y}, \mathbf{p}_r) \\
&= \Re \{ \sum_{\omega} \omega^4 \sum_{\mathbf{x}_s} |f_s(\omega)|^2 G(\mathbf{x}, \mathbf{x}_s, \omega) G^*(\mathbf{y}, \mathbf{x}_s, \omega) \\
&\times \sum_{\mathbf{x}_r} w(\mathbf{x}_r, \mathbf{x}_s) G(\mathbf{x}, \mathbf{x}_r, \omega) \alpha(\mathbf{x}_r, \mathbf{p}_r, \omega) \\
&\times \sum_{\mathbf{x}'_r} w(\mathbf{x}'_r, \mathbf{x}_s) G^*(\mathbf{y}, \mathbf{x}'_r, \omega) \alpha^*(\mathbf{x}'_r, \mathbf{p}_r, \omega) \; \} ,
\end{aligned} \tag{8}$$

where we introduce an extra summation $\sum_{\mathbf{x}'_r}$ for the receiver-side Green's functions, and $\alpha(\mathbf{x}_r, \mathbf{p}_r, \omega)$ is some weighting function, or more specifically, encoding function, to be specified later. Hereafter, $\widetilde{H}(\mathbf{x}, \mathbf{y}, \mathbf{p}_r)$ is referred as the receiver-side phase-encoded Hessian. Though $\widetilde{H}(\mathbf{x}, \mathbf{y}, \mathbf{p}_r)$ can be computed in a way similar to the direct implementation of the exact Hessian as defined by equation 7, it offers more flexibility and can be efficiently computed without explicitly saving the Green's functions.

Because of the linearity of the wave equation, the term $\sum_{\mathbf{x}_r} w(\mathbf{x}_r, \mathbf{x}_s) G(\mathbf{x}, \mathbf{x}_r, \omega) \alpha(\mathbf{x}_r, \mathbf{p}_r, \omega)$ now becomes the extrapolated wavefield at image point $\mathbf{x}$. It corresponds to the composite source $f_c(x, y, \mathbf{x}_s, \mathbf{p}_r, \omega)$ on the surface that can be defined as follows:

$$\begin{aligned}
&f_c(x, y, \mathbf{x}_s, \mathbf{p}_r, \omega) \\
&= \sum_{\mathbf{x}_r} w(\mathbf{x}_r, \mathbf{x}_s) \delta(x - x_r, y - y_r) \alpha(\mathbf{x}_r, \mathbf{p}_r, \omega),
\end{aligned} \tag{9}$$

where $\delta(x - x_r, y - y_r)$ is the Dirac delta function centered at $\mathbf{x}_r = (x_r, y_r)$ and can be considered as a point source on the surface. Hence, the composite source is obtained by linearly combining point sources at all receiver locations for a specific shot located at $\mathbf{x}_s$.

The function $\alpha(\mathbf{x}_r, \mathbf{p}_r, \omega)$ serves as a weight when combining these point sources. The same thing holds for the other summation term, $\sum_{\mathbf{x}'_r} w(\mathbf{x}'_r, \mathbf{x}_s) G^*(\mathbf{x}'_r, \mathbf{y}, \omega) \alpha^*(\mathbf{x}'_r, \omega)$, except that it is the complex conjugate of the same extrapolated wavefield at a neighbor image point $\mathbf{y}$. To make it clearer, we define a receiver wavefield $R(\mathbf{x}, \mathbf{x}_s, \mathbf{p}_r, \omega)$ corresponding to the receiver composite source $f_c(x, y, \mathbf{x}_s, \mathbf{p}_r, \omega)$ as

$$R(\mathbf{x}, \mathbf{x}_s, \mathbf{p}_r, \omega) = \sum_{\mathbf{x}_r} w(\mathbf{x}_r, \mathbf{x}_s) G(\mathbf{x}_r, \mathbf{x}, \omega) \alpha(\mathbf{x}_r, \mathbf{p}_r, \omega), \tag{10}$$

and a source wavefield corresponding to a point source located at $\mathbf{x}_s$ on the surface as

$$S(\mathbf{x}, \mathbf{x}_s, \omega) = f_s(\omega) G(\mathbf{x}, \mathbf{x}_s, \omega). \tag{11}$$

Substituting equations 10 and 11 into equation 8 leads to

$$\begin{aligned} \widetilde{H}(\mathbf{x}, \mathbf{y}, \mathbf{p}_r) &= \Re \{ \sum_{\omega} \omega^4 \sum_{\mathbf{x}_s} S(\mathbf{x}, \mathbf{x}_s, \omega) S^*(\mathbf{y}, \mathbf{x}_s, \omega) \\ &\times R(\mathbf{x}, \mathbf{x}_s, \mathbf{p}_r, \omega) R^*(\mathbf{y}, \mathbf{x}_s, \mathbf{p}_r, \omega) \} , \end{aligned} \tag{12}$$

which means $\widetilde{H}(\mathbf{x}, \mathbf{y}, \mathbf{p}_r)$ can be computed by crosscorrelating the source and receiver wavefields with their shifted complex conjugates ($\mathbf{y}$ is a neighborhood point around $\mathbf{x}$). Therefore, the algorithm for computing the receiver-side phase-encoded Hessian is similar to the wave-equation shot-profile migration algorithm, except that the boundary condition for the receiver wavefield and the imaging condition are slightly modified. In the shot-profile migration, the boundary condition for the receiver wavefield is the recorded data, and we crosscorrelate the source wavefield and the receiver wavefield to produce the image; here, in contrast, we use the composite source as the boundary condition for the receiver wavefield, and then invoke the imaging condition defined by equation 12 to produce the new operator $\widetilde{H}(\mathbf{x}, \mathbf{y}, \mathbf{p}_r)$. In other words, we do not have to save the Green's functions at all. Computing $\widetilde{H}(\mathbf{x}, \mathbf{y}, \mathbf{p}_r)$ is also efficient because multiple Green's functions are computed at the same time during the wavefield extrapolation.

We can stack $\widetilde{H}(\mathbf{x},\mathbf{y},\mathbf{p}_r)$ over $\mathbf{p}_r$ and after some simple algebraic manipulation, we obtain:

$$\begin{aligned}
\widetilde{H}(\mathbf{x},\mathbf{y}) &= \sum_{\mathbf{p}_r} \widetilde{H}(\mathbf{x},\mathbf{y},\mathbf{p}_r) \\
&= \Re\{ \sum_{\omega} \omega^4 \sum_{\mathbf{x}_s} |f_s(\omega)|^2 G(\mathbf{x},\mathbf{x}_s,\omega) G^*(\mathbf{y},\mathbf{x}_s,\omega) \\
&\times \sum_{\mathbf{x}_r} w(\mathbf{x}_r,\mathbf{x}_s) G(\mathbf{x},\mathbf{x}_r,\omega) G^*(\mathbf{y},\mathbf{x}_r,\omega) \sum_{\mathbf{p}_r} |\alpha(\mathbf{x}_r,\mathbf{p}_r,\omega)|^2 \\
&+ \sum_{\omega} \omega^4 \sum_{\mathbf{x}_s} |f_s(\omega)|^2 G(\mathbf{x},\mathbf{x}_s,\omega) G^*(\mathbf{y},\mathbf{x}_s,\omega) \\
&\times \sum_{\mathbf{x}_r} \sum_{\mathbf{x}'_r \neq \mathbf{x}_r} w(\mathbf{x}_r,\mathbf{x}_s) G(\mathbf{x},\mathbf{x}_r,\omega) w(\mathbf{x}'_r,\mathbf{x}_s) G^*(\mathbf{y},\mathbf{x}'_r,\omega) \\
&\times \sum_{\mathbf{p}_r} \alpha(\mathbf{x}_r,\mathbf{p}_r,\omega) \alpha^*(\mathbf{x}'_r,\mathbf{p}_r,\omega) \}. \qquad (13)
\end{aligned}$$

If we let the weighting function satisfy $\sum_{\mathbf{p}_r} |\alpha(\mathbf{x}_r,\mathbf{p}_r,\omega)|^2 = 1$, the first term in equation 13 becomes the exact Hessian $H(\mathbf{x},\mathbf{y})$ (equation 7); however, if the second term cannot be removed, it becomes undesired crosstalk from the crosscorrelations among different receiver-side Green's functions and we obtain:

$$\widetilde{H}(\mathbf{x},\mathbf{y}) = H(\mathbf{x},\mathbf{y}) + \text{Crosstalk}. \qquad (14)$$

Simultaneous encoding of the source- and receiver-side Green's functions

We can further encode the source-side Green's function by synthesizing composite sources from the source locations. For simplicity, we assume OBS or land acquisition geometries, where all shots have the same receiver spread. Therefore, we have the following relation:

$$w(\mathbf{x}_r,\mathbf{x}_s) = w_r(\mathbf{x}_r) w_s(\mathbf{x}_s), \qquad (15)$$

where $w_r(\mathbf{x}_r)$ and $w_s(\mathbf{x}_s)$ define the ranges of receivers and sources for a given acquisition geometry. With the above assumption, we can construct a simultaneously phase-encoded

Hessian as follows:

$$\begin{aligned}\widetilde{\widetilde{H}}(\mathbf{x},\mathbf{y},\mathbf{p}_s,\mathbf{p}_r) &= \Re\{\sum_{\omega}\omega^4 \\ &\times \sum_{\mathbf{x}_s} w_s(\mathbf{x}_s) f_s(\omega) G(\mathbf{x},\mathbf{x}_s,\omega)\beta(\mathbf{x}_s,\mathbf{p}_s,\omega) \\ &\times \sum_{\mathbf{x}'_s} w_s(\mathbf{x}'_s) f^*_s(\omega) G^*(\mathbf{y},\mathbf{x}'_s,\omega)\beta^*(\mathbf{x}'_s,\mathbf{p}_s,\omega) \\ &\times \sum_{\mathbf{x}_r} w_r(\mathbf{x}_r) G(\mathbf{x},\mathbf{x}_r,\omega)\alpha(\mathbf{x}_r,\mathbf{p}_r,\omega) \\ &\times \sum_{\mathbf{x}'_r} w_r(\mathbf{x}'_r) G^*(\mathbf{y},\mathbf{x}'_r,\omega)\alpha^*(\mathbf{x}'_r,\mathbf{p}_r,\omega)\ \}. \end{aligned} \tag{16}$$

where we introduce two extra summations: $\sum_{\mathbf{x}'_s}$ for the source-side Green's functions and $\sum_{\mathbf{x}'_r}$ for the receiver-side Green's functions. Similar to $\alpha(\mathbf{x}_r,\mathbf{p}_r,\omega)$, $\beta(\mathbf{x}_s,\mathbf{p}_s,\omega)$ is also a weighting function and will be specified later. Let us once again define the composite source wavefield $S(\mathbf{x},\mathbf{p}_s,\omega)$ and composite receiver wavefield $R(\mathbf{x},\mathbf{p}_r,\omega)$ as follows:

$$S(\mathbf{x},\mathbf{p}_s,\omega) = \sum_{\mathbf{x}_s} w_s(\mathbf{x}_s) f_s(\omega) G(\mathbf{x},\mathbf{x}_s,\omega)\beta(\mathbf{x}_s,\mathbf{p}_s,\omega), \tag{17}$$

and

$$R(\mathbf{x},\mathbf{p}_r,\omega) = \sum_{\mathbf{x}_r} w_r(\mathbf{x}_r) G(\mathbf{x},\mathbf{x}_r,\omega)\alpha(\mathbf{x}_r,\mathbf{p}_r,\omega). \tag{18}$$

Substituting equations 17 and 18 into equation 16 leads to

$$\begin{aligned}\widetilde{\widetilde{H}}(\mathbf{x},\mathbf{y},\mathbf{p}_s,\mathbf{p}_r) &= \Re\{\sum_{\omega}\omega^4 S(\mathbf{x},\mathbf{p}_s,\omega)S^*(\mathbf{y},\mathbf{p}_s,\omega) \\ &\times R(\mathbf{x},\mathbf{p}_r,\omega)R^*(\mathbf{y},\mathbf{p}_r,\omega)\ \}. \end{aligned} \tag{19}$$

Therefore, computing the simultaneously phase-encoded Hessian $\widetilde{\widetilde{H}}(\mathbf{x},\mathbf{y},\mathbf{p}_s,\mathbf{p}_r)$ requires only two wavefield propagations: one for the composite source wavefield defined by equation 17, and the other for the composite receiver wavefield defined by equation 18.

Similar to the case of the receiver-side phase-encoded Hessian, we can stack $\widetilde{\widetilde{H}}(\mathbf{x},\mathbf{y},\mathbf{p}_s,\mathbf{p}_r)$ over both $\mathbf{p}_s$ and $\mathbf{p}_r$. If the weighting functions satisfy $\sum_{\mathbf{p}_r}|\alpha(\mathbf{x}_r,\mathbf{p}_r,\omega)|^2 = 1$ and

$\sum_{\mathbf{p}_s} |\beta(\mathbf{x}_s, \mathbf{p}_s, \omega)|^2 = 1$, the stacked result $\widetilde{\widetilde{H}}(\mathbf{x}, \mathbf{y})$ becomes the sum of the exact Hessian and the crosstalk:

$$\begin{aligned} \widetilde{\widetilde{H}}(\mathbf{x}, \mathbf{y}) &= \sum_{\mathbf{p}_s} \sum_{\mathbf{p}_r} \widetilde{\widetilde{H}}(\mathbf{x}, \mathbf{y}, \mathbf{p}_s, \mathbf{p}_r) \\ &= H(\mathbf{x}, \mathbf{y}) + \text{Crosstalk}. \end{aligned} \tag{20}$$

Thus, by encoding the Green's functions for the Hessian computation, we face a situation similar to that encountered in phase-encoding migration (Romero et al., 2000; Liu et al., 2006), i.e., our exact Hessian is contaminated by crosstalk artifacts, so we seek to define weighting functions $\alpha(\mathbf{x}_r, \mathbf{p}_r, \omega)$ and $\beta(\mathbf{x}_s, \mathbf{p}_s, \omega)$ that attenuate the crosstalk as much as possible. In the next two sections, I examine two different phase-encoding schemes to attenuate the crosstalk, namely, plane-wave-phase encoding and random-phase encoding.

Plane-wave-phase encoding

Suppose we choose the weighting functions to be

$$\alpha(\mathbf{x}_r, \mathbf{p}_r, \omega) = A_r(\omega) \mathrm{e}^{i\omega \mathbf{p}_r \cdot \mathbf{x}_r}, \tag{21}$$

$$\beta(\mathbf{x}_s, \mathbf{p}_s, \omega) = A_s(\omega) \mathrm{e}^{i\omega \mathbf{p}_s \cdot \mathbf{x}_s}, \tag{22}$$

which are the well known plane-wave or delayed-shot phase-encoding functions (Whitmore, 1995; Zhang et al., 2005; Liu et al., 2006), where $i = \sqrt{-1}$, $A_r(\omega)$ and $A_s(\omega)$ are real functions depending upon the angular frequency ω; and $\mathbf{p}_r = (p_{r_x}, p_{r_y})$ and $\mathbf{p}_s = (p_{s_x}, p_{s_y})$ are the ray parameters for the receiver and source plane waves on the surface, respectively. As proved by Liu et al. (2006), in continuous case, integrating over plane waves completely attenuates the crosstalk in the plane-wave source migration, and the final migration result is exactly equivalent to the standard shot-profile migration re-

sult. The same property holds here in the scenario of Hessian computation, as proved in Appendix A and B: integrating over $\mathbf{p}_r$ and $\mathbf{p}_s$, and choosing $A_r(\omega)$ and $A_s(\omega)$ to satisfy $A_r^2(\omega) = |\omega|$, $A_s^2(\omega) = |\omega|$ in 2-D and $A_r^2(\omega) = |\omega|^2$, $A_s^2(\omega) = |\omega|^2$ in 3-D, asymptotically, we have $\sum_{\mathbf{p}_r} \alpha(\mathbf{x}_r, \mathbf{p}_r, \omega)\alpha^*(\mathbf{x}'_r, \mathbf{p}_r, \omega)$ and $\sum_{\mathbf{p}_s} \beta(\mathbf{x}_s, \mathbf{p}_s, \omega)\beta^*(\mathbf{x}'_s, \mathbf{p}_s, \omega)$ equal 1 (if $\mathbf{x}_r = \mathbf{x}'_r$, $\mathbf{x}_s = \mathbf{x}'_s$) and 0 (if $\mathbf{x}_r \neq \mathbf{x}'_r$, $\mathbf{x}_s \neq \mathbf{x}'_s$). Hence the crosstalk in both equations 14 and 20 becomes zero, and the approximate Hessians $\widetilde{H}(\mathbf{x}, \mathbf{y})$ and $\widetilde{\widetilde{H}}(\mathbf{x}, \mathbf{y})$ converge to the exact Hessian $H(\mathbf{x}, \mathbf{y})$. In the discrete form used in practice, the number of $\mathbf{p}_s$ and $\mathbf{p}_r$ values can be chosen in a way similar to those discussed by Stork and Kapoor (2004); Zhang et al. (2005); Etgen (2005); Stork and Kapoor (2006); Zhang et al. (2006).

Random-phase encoding

Instead of using the plane-wave-phase encoding function, we can use random phases to disperse unwanted crossterms (Romero et al., 2000). The weighting functions can be chosen as follows:

$$\alpha(\mathbf{x}_r, \mathbf{p}_r, \omega) = \frac{1}{\sqrt{N_{\text{realize}}}} \mathrm{e}^{i\gamma(\mathbf{x}_r, \mathbf{p}_r, \omega)}, \tag{23}$$

$$\beta(\mathbf{x}_s, \mathbf{p}_s, \omega) = \frac{1}{\sqrt{N_{\text{realize}}}} \mathrm{e}^{i\gamma(\mathbf{x}_s, \mathbf{p}_s, \omega)}, \tag{24}$$

where the phase functions $\gamma(\mathbf{x}_r, \mathbf{p}_r, \omega)$ and $\gamma(\mathbf{x}_s, \mathbf{p}_s, \omega)$ are sequences of random numbers between 0 and 2π, they are random functions of both space and frequency; the parameters $\mathbf{p}_r$ and $\mathbf{p}_s$ now define the indexes of different realizations of the random sequences; N_{realize} is the number of realizations. Obviously, the weighting functions satisfy $\sum_{\mathbf{p}_r} |\alpha(\mathbf{x}_r, \mathbf{p}_r, \omega)|^2 = 1$ and $\sum_{\mathbf{p}_s} |\beta(\mathbf{x}_s, \mathbf{p}_s, \omega)|^2 = 1$, therefore, the encoded Hessian has the same form as in equation 14 (receiver-side encoded Hessian) or 20 (simultaneously encoded Hessian). Because the phases of the crosstalk are randomized, when we sum over frequencies, sources and receivers

to generate the final result, the phases of the crosstalk will not agree with each other, and consequently, the crosstalk will be attenuated by stacking. To maximize the phase differences, a uniformly distributed random sequence could be used (Romero et al., 2000). To further attenuate the crosstalk, multiple realizations of the random sequences can be used ($N_{\text{realize}} > 1$): the randomly phase-encoded Hessian is computed multiple times with different realizations of the random-phase function and then stacked together to produce the final result. The cost of this process is linearly proportional to the number of realizations.

Cost comparison

In this section, I compare the cost for different methods to determine the savings generated by using the phase-encoding method. As discussed before, Hessian computation contains two main parts: wavefield propagation (Green's functions) and crosscorrelation among different Green's functions. Since the crosscorrelation parts are similar for methods with or without phase encoding, I will only compare the cost for the first part, i.e, wavefield propagation for Green's functions. I consider general 3-D cases; for 2-D applications, the cost for each method can also be conveniently obtained by setting the corresponding crossline parameter(s) (with subscript $_y$) to 1.

Let us assume a 3-D seismic survey that has N_s shots in total, covering a surface area that can be divided into $N_x \times N_y$ cells; and our target area for inversion is a 3-D cube with M_x, M_y and M_z samples in x, y and z directions. Table 1 illustrates the cost comparison for a marine acquisition geometry, while Table 2 compares the cost for an OBS or a land acquisition geometry. Since simultaneous phase encoding is derived under an OBS or a land acquisition geometry, Table 1 only compares the cost of the receiver-side encoding

method with that of the direct method. In both tables, N_ω is the number of frequencies of the wavefield, $N_{p_{s_x}}$ and $N_{p_{s_y}}$ are the numbers of source ray parameters for the inline and crossline directions, and $N_{p_{r_x}}$ and $N_{p_{r_y}}$ are the numbers of receiver ray parameters for the inline and crossline directions, respectively. N_{realize} is the number of realizations of the random sequences, the same as that defined in the previous section.

From both tables, we can find that the simultaneous random-phase encoding is the most efficient method for an OBS or a land acquisition geometry, which requires only $2N_\omega$ wavefield propagations for one realization. If a marine acquisition geometry is used, it would be efficient to use the receiver-side random-phase encoding (if $N_s < N_x N_y$); the cost for one realization is comparable to that of a shot-profile migration. Plane-wave phase-encoding methods, however, may potentially need more wavefiled propagations than the direct method, depending on how many plane waves are used for computing the Hessian. Also note that the phase-encoding methods do not require storage of any Green's functions, which is a crucial benefit for large-scale applications, since the size of the Green's functions ($M_x M_y M_z N_x N_y N_\omega$) can easily reach an unaffordably large number. For example, for a target area with size $M_x = M_y = M_z = 100$ and survey area with size $N_x = N_y = 1000$, the Green's functions for a single frequency ($N_\omega = 1$) is about 8 terabytes (8 comes from the fact that the Green's function is a complex value).

NUMERICAL EXAMPLES

In this section, I show several numerical examples for two different velocity models. The first is a simple constant-velocity model, which I use to verify the proposed algorithms for computing the Hessian; the second is the more complicated Sigsbee2A velocity model (Paffenholz et al., 2002). Because of the complex salt body and limited acquisition geometry,

there are shadow zones under the salt where conventional wave-equation migration algorithms often fail to produce reliable images. Therefore, it is useful to test if inversion by using the phase-encoded Hessian can improve the final image.

Verification of the algorithm: a constant velocity model

I verify the proposed phase-encoding algorithms on a constant velocity model ($v = 2$ km/s) for several different acquisition geometries. Figure 1 shows the diagonal part of the Hessian (when $\mathbf{x} = \mathbf{y}$) for an acquisition geometry containing one shot at -0.6 km and two receivers located at 0.6 km and 1.2 km on the surface. A ricker wavelet with a 20 Hz dominant frequency is used as the source function, and frequencies from 5 Hz to 35 Hz are used to generate the following results. Figure 1a is the exact diagonal of the Hessian, uncontaminated by any crosstalk artifacts. Figure 1b shows the Hessian with crosstalk, which is obtained using equation 8 with $\alpha(\mathbf{x}_r, \mathbf{p}_r, \omega) = 1$; the crosstalk can be easily identified as the vertical stripes on the right side of the image. Figure 1c is the receiver-side plane-wave phase-encoded Hessian with 31 plane waves stacked together. The crosstalk has been successfully removed, and Figure 1c looks very similar to Figure 1a. Figure 1d shows the receiver-side randomly phase-encoded Hessian with one random realization; the crosstalk is dispersed throughout the image. Figure 1e and Figure 1f show the results for 5 and 20 random realizations; as expected, the crosstalk is better attenuated by using more random realizations.

Figure 2 shows the Hessian with off-diagonals (with size 81×81) at the image point $x = 0.5$ km, $z = 1.5$ km. The acquisition geometry is the same as that in Figure 1. The horizontal and vertical axes in Figure 2 denote the horizontal and vertical offsets away from

the image point $x = 0.5$ km, $z = 1.5$ km. Figure 2a shows the exact Hessian. Since the illumination in the subsurface is very poor (only one source and two receivers), we can observe two events intersecting at the origin (the diagonal element of the Hessian) and spreading out over the off-diagonals. When more sources and receivers are used, i.e., with better subsurface illumination, the energy in the local Hessian operator would be more focused at the origin (as illustrated in the subsequent examples). Figure 2b is the Hessian with crosstalk, where two extra undesired events present in the operator; Figure 2c shows the receiver-side plane-wave phase-encoded Hessian, plane-wave-phase encoding successfully attenuates the crosstalk; Figures 2d, 2e and 2f show the receiver-side randomly phase-encoded Hessian with different number of realizations.

In the next example, I change the acquisition geometry used in the previous example from 2 receivers to 401 receivers. The receivers range from -2 km to 2 km, with a spacing of 0.01 km. The source location is changed to -1 km. Once again, Figure 3 shows the diagonal part of the Hessian operator, while Figure 4 illustrates the off-diagonals at the image point $x = 0.5$ km, $z = 1.5$ km in the subsurface. Since the receiver spread is asymmetric with respect to the source location, the energy in the exact diagonal of Hessian (Figure 3a) is slightly tilted towards the right and the energy in the local Hessian operator shown in Figure 4a is well focused due to contributions from many receivers. However, when the Hessian is contaminated by crosstalk, the energy in the diagonal of the Hessian (Figure 3b) shows wrong orientation and the illumination pattern is very different from the correct one (Figure 3a); the local Hessian operator shown in Figure 4b is also far from focusing. The crosstalk is successfully attenuated by the proposed phase-encoding techniques, as shown in Figure 3c and Figure 4c for the receiver-side plane-wave-phase encoding (31 receiver-side plane waves are used), and Figure 3d and Figure 4d for the receiver-side random-phase

encoding with one realization. Although the crosstalk is greatly suppressed in Figure 3d and Figure 4d, some random noise appears in the background, which is caused by the random nature of the phase-encoding function. The random noise can be further suppressed by using more random realizations. Figure 3e, Figure 4e and Figure 3f, Figure 4f show the results with 5 and 20 random realizations, respectively. The crosstalk is greatly attenuated.

Instead of computing more random realizations, which may substantially increase the cost, we can use the fact that the randomized crosstalk can be well attenuated when many sources are used (this is almost always true in practice, where thousands of shots are often fired in acquiring field seismic data). Because the phase function is random both in space and frequency, stacking over more sources makes the phases of the crosstalk more inconsistent with each other, hence better suppresses these artifacts. Figure 5 and Figure 6 show examples when many sources are used for the same constant velocity model. In this case, a land acquisition geometry is used, where the receiver locations are fixed for all shots. The receiver location is the same as in the previous example, but now we have 401 shots from -2 km to 2 km with a 0.01 km spacing. Figure 5a shows the exact diagonal of the Hessian, while Figure 5b shows the diagonal of the receiver-side randomly phase-encoded Hessian with only one realization. As apposed to the previous example (Figure 3d), the crosstalk is greatly attenuated even with one random realization. Figure 6 compares the off-diagonals of the Hessian for the image point located at $x = 0.5$ km and $z = 1.5$ km; as we can see from the comparison, even with only one realization, the encoded Hessian is almost identical to the exact Hessian.

Application of the phase-encoded Hessian: Sigsbee2A model

To demonstrate an application of the explicit Hessian operator, I apply the model-space inversion approach to the Sigsbee2A model (Paffenholz et al., 2002). Figure 7 shows the stratigraphic velocity model, which has been used for migration and Hessian computation. The original data is modeled using two-way wave equation with a marine type acquisition geometry, where the receiver spread is moving along with the source (Paffenholz et al., 2002). There are 500 shots in total and the maximum offset for each shot is about 8 km. Though the data is modeled with two-way wave equation, in the following examples, one-way wave-equation-based Fourier finite-difference (FFD) (Ristow and Rühl, 1994) propagator is used for both migration and phase-encoded Hessian computation. The explicit Hessian operator is computed using the receiver-side random-phase encoding method with the frequency band from 5 Hz to 35 Hz, equivalent to that of the migrated image $\mathbf{m}_{\text{mig}}$. Only one realization has been used; because the number of shots is big, one realization is sufficient to provide reasonably good suppression of the crosstalk.

I use two different strategies of applying the explicit Hessian operator: the first is to compute only the diagonal of the Hessian operator and use it as a weight to normalize the migrated image; this is often known as the normalized migration (Rickett, 2003) or amplitude-preserving migration (Plessix and Mulder, 2004). The other strategy is to compute a limited number of Hessian off-diagonals, and then iteratively minimize the model-space objective function $J(\mathbf{m})$ (equation 6) to find an optimum reconstruction of the reflectivity $\mathbf{m}$. In this example, the number of the off-diagonal elements is chosen by trial and error and each local Hessian filter has 21×21 elements, the size of which seems to be big enough to capture most of the energy even for poorly illuminated areas. A linear conjugate-gradient solver

and a simple damping regularization that minimizes the energy of the model parameters are used for the model-space iterative inversion.

Normalized migration

Figure 8 shows the diagonal of the receiver-side randomly phase-encoded Hessian. Note the uneven illumination below the salt caused by the complex salt body and limited acquisition geometry. For comparison, Figure 9 shows the source-wavefield intensity, computed using $H_{SI}(\mathbf{x},\mathbf{x}) = \Re\{ \sum_\omega \omega^4 \sum_{\mathbf{x}_s} |f_s(\omega)G(\mathbf{x},\mathbf{x}_s,\omega)|^2 \}$. $H_{SI}(\mathbf{x},\mathbf{x})$ is a crude approximation to the exact diagonal of Hessian, because it assumes the constant receiver-side Green's functions and ignores the effects of the limited receiver aperture. It over-estimates the total energy that enters the earth and returns to be recorded by the receivers. This is why Figure 9 shows stronger, but less accurate, illumination below the salt.

Figure 10 shows the conventional one-way wave-equation shot-profile migrated image, where the unbalanced amplitudes caused by uneven illumination below the salt are easily identified. Figure 11 and Figure 12 show the migrated image normalized with the diagonal of the phase-encoded Hessian (Figure 8) and the source-wavefield intensity (Figure 9), respectively. All three figures are plotted with the same scale. Figure 11 shows more balanced amplitudes across the section than Figure 12, especially in areas below the salt. However, also note that normalized migration does not help improve the resolution of the image, this is because the diagonal of the Hessian only serves as a scaling factor, it has little deconvolution effects. The resolution can be improved by using the off-diagonal elements of the Hessian matrix as shown in the subsequent examples.

Target-oriented inversion

The model-space target-oriented inversion is performed to a selected area below the salt. Figure 13 shows the receiver-side randomly phase-encoded Hessian operator for the particular region of interest: Figure 13a shows the diagonal part of the Hessian operator; Figure 13b is obtained by convolving the Hessian operator (21×21 in size) with a collection of point scatterers (impulse responses). It demonstrates the varying shapes and non-stationarities of the Hessian operators across the section. Note that in well-illuminated areas, the Hessian operator is well focused, while in poorly illuminated areas, the Hessian operator is tilted and smeared and has a preferred dipping orientation, which means these image points are illuminated by only a few dip angles (Gelius et al., 2002).

Figure 14 shows the comparison between migration and inversion: Figure 14a is the migrated image, and Figure 14b is the inverted image obtained using the randomly phase-encoded Hessian operator. The result is obtained after 20 iterations of the linear conjugate-gradient method. Figure 15 plots the normalized residual as a function of iteration number; the residual converges after about 12 iterations. In the inversion result, the effects of uneven illumination are corrected, the inverted image looks slightly sharper and crisper than the migrated image; the shadow zones that in the migrated image are now filled in with structures (circled areas), and the sediments (the area outlined by the top circle) and the dipping faults (indicated with arrows) extend much closer to the salt body. The improved image helps locate sediment truncations against salt, which are important in finding subsalt structural traps. For comparison, Figure 14c shows the filtered true reflectivity.

A closeup comparison for areas around the point diffractors is shown in Figure 16. Figure 17 compares the amplitude spectrum of the migrated image (Figure 16a) and the

inverted image (Figure 16b); the inverted image shows a broader range of spatial frequencies, suggesting slightly improved spatial resolution. Figure 18 shows a horizontal trace located at depth level 5.1892 km (slicing through the diffractors) extracted from different images shown in Figure 16. The inverted result (the dashed line) better predicts the true reflectivity (the dotted line) than the migrated result (the solid line).

DISCUSSION

The model-space inversion approach, which requires building the Hessian operator $\mathbf{L}^*\mathbf{L}$, squares the condition number of the Born modeling operator $\mathbf{L}$. Generally speaking, the Hessian is often ill-conditioned, and inverting the Hessian is sensitive to roundoff errors. Hence, regularization should be used to stabilize the inversion process.

The inverted image, Figure 14b, also shows increased noise, for example, at around horizontal distance 11 km and depth level 4 km, where the illumination is extremely poor. This is partially due to the null space of the Hessian operator. Another possible contribution might be the randomized crosstalk introduced in the randomly phase-encoded Hessian. This can be a concern, since the accuracy of the Hessian may affect the convergence of inversion. However, a small amount of random noise in the operator might also be useful if one considers it as a random regularization, hence, it may have the chance to improve the condition number of the Hessian operator, making it easier to invert. How the crosstalk affects the inversion is still not very clear and is beyond the scope of this paper; it remains a research area for further investigation. To suppress the noise, more sophisticated regularization that better predicts the inverse of the model covariance, such as roughening along reflection angles (Kuhl and Sacchi, 2003; Clapp, 2005) or geological dips (Prucha and Biondi, 2002; Clapp, 2005), can be introduced in the inversion process.

The least-squares inversion approach assumes an accurate background velocity model is known, which, however, is not always true in practice. Therefore, future research should test the sensitivity of the inversion approach to velocity errors. The theory also assumes single scattering (Born approximation), other coherent energy, such as multiple, does not fit into this inversion framework. In the Sigsbee2A example, the internal multiple at around $x = 11.6$ km and $z = 4.2$ km in the migrated image (Figure 14a) becomes even more pronounced in the inverted image (Figure 14b). Hence, multiple suppression is suggested prior to inversion.

CONCLUSIONS

I present a method based on phase encoding that allows efficient computation of the explicit Hessian operator for the wave-equation least-squares migration/inversion problem. The proposed algorithm does not require storing Green's functions, which is often too big to be affordable in practice. Hence, the phase-encoded Hessian has the potential to be applied to large-scale problems at a lower cost. Although this paper demonstrates examples with one-way wave equation, the theory for computing the phase-encoded Hessian is not limited to one-way wave equation. Two-way wave equation can also be used in a similar way to compute the phase-encoded Hessian, which may bring even more savings in computational cost. The phase-encoded Hessian via two-way wave equation may also be applied as a preconditioner for the full waveform inversion problem.

The target-oriented inversion examples on the Sigsbee2A model show that wave-equation least-squares migration/inversion can partially correct the effects of uneven illumination, and it can produce an image with more balanced amplitudes and slightly higher spatial resolution to that produced by migration, especially in areas with low illumination and

shadow zones. Thus it provides a good tool for imaging complex geologies.

ACKNOWLEDGMENTS

I thank Alejandro Valenciano and Biondo Biondi for enlightening discussions. I thank the sponsors of the Stanford Exploration Project for their support, and I acknowledge SMAART JV for providing the Sigsbee2A data set. I also thank the Associate Editor Isabelle Lecomte, Gerrit Toxopeus and two anonymous reviewers, whose comments and suggestions significantly improve the quality of this paper.

APPENDIX A

PROOF OF CONVERGENCE OF THE RECEIVER-SIDE PLANE-WAVE PHASE-ENCODED HESSIAN

This appendix demonstrates that the receiver-side plane-wave phase-encoded Hessian $\widetilde{H}(\mathbf{x},\mathbf{y},\mathbf{p}_r)$ converges to the exact Hessian $H(\mathbf{x},\mathbf{y})$ by integrating over receiver ray parameters. Using the plane-wave phase-encoding functions, the approximate Hessian for a single $\mathbf{p}_r = (p_{r_x}, p_{r_y})$ takes the form:

$$\begin{aligned}
&\widetilde{H}(\mathbf{x},\mathbf{y},\mathbf{p}_r) \\
&= \Re\{ \sum_{\omega} \omega^4 \sum_{\mathbf{x}_s} |f_s(\omega)|^2 A_r^2(\omega) G(\mathbf{x},\mathbf{x}_s,\omega) G^*(\mathbf{y},\mathbf{x}_s,\omega) \\
&\times \sum_{\mathbf{x}_r} w(\mathbf{x}_r,\mathbf{x}_s) G(\mathbf{x},\mathbf{x}_r,\omega) \mathrm{e}^{i\omega \mathbf{p}_r\cdot\mathbf{x}_r} \\
&\times \sum_{\mathbf{x}'_r} w(\mathbf{x}'_r,\mathbf{x}_s) G^*(\mathbf{y},\mathbf{x}'_r,\omega) \mathrm{e}^{-i\omega \mathbf{p}_r\cdot\mathbf{x}'_r} \}\,. \qquad \text{(A-1)}
\end{aligned}$$

Integrating over $\mathbf{p}_r$ from $-\infty$ to $+\infty$, and changing the order of integration and summation, we have

$$\begin{aligned}
\widetilde{H}(\mathbf{x},\mathbf{y}) &= \int_{-\infty}^{+\infty} \widetilde{H}(\mathbf{x},\mathbf{y},\mathbf{p}_r)d\mathbf{p}_r \\
&= \Re\{ \sum_{\omega} \omega^4 \sum_{\mathbf{x}_s} |f_s(\omega)|^2 A_r^2(\omega) G(\mathbf{x},\mathbf{x}_s,\omega) G^*(\mathbf{y},\mathbf{x}_s,\omega) \\
&\times \sum_{\mathbf{x}_r} w(\mathbf{x}_r,\mathbf{x}_s) G(\mathbf{x},\mathbf{x}_r,\omega) \sum_{\mathbf{x}'_r} w(\mathbf{x}'_r,\mathbf{x}_s) G^*(\mathbf{y},\mathbf{x}'_r,\omega) \\
&\times \int_{-\infty}^{+\infty} \mathrm{e}^{-i\omega\mathbf{p}_r\cdot(\mathbf{x}'_r-\mathbf{x}_r)} d\mathbf{p}_r \,\}. \qquad \text{(A-2)}
\end{aligned}$$

Note that

$$\int_{-\infty}^{+\infty} \mathrm{e}^{-i\omega\mathbf{p}_r\cdot(\mathbf{x}'_r-\mathbf{x}_r)} d\mathbf{p}_r = \frac{1}{|\omega|}\delta(\mathbf{x}'_r-\mathbf{x}_r) \qquad \text{(A-3)}$$

in 2-D and

$$\int_{-\infty}^{+\infty} \mathrm{e}^{-i\omega\mathbf{p}_r\cdot(\mathbf{x}'_r-\mathbf{x}_r)} d\mathbf{p}_r = \frac{1}{|\omega|^2}\delta(\mathbf{x}'_r-\mathbf{x}_r) \qquad \text{(A-4)}$$

in 3-D. Thus, if we choose the real function $A_r(\omega)$ such that it satisfies $A_r^2(\omega) = |\omega|$ in 2-D and $A_r^2(\omega) = |\omega|^2$ in 3-D, then we get

$$\widetilde{H}(\mathbf{x},\mathbf{y}) = H(\mathbf{x},\mathbf{y}). \qquad \text{(A-5)}$$

APPENDIX B

PROOF OF CONVERGENCE OF THE SOURCE- AND RECEIVER-SIDE SIMULTANEOUSLY PLANE-WAVE PHASE-ENCODED HESSIAN

This appendix demonstrates that the simultaneously plane-wave phase-encoded Hessian $\widetilde{\widetilde{H}}(\mathbf{x},\mathbf{y},\mathbf{p}_s,\mathbf{p}_r)$ converges to the exact Hessian $H(\mathbf{x},\mathbf{y})$ by integrating over both source and receiver ray parameters. The simultaneously plane-wave phase-encoded Hessian takes the

form

$$
\begin{aligned}
&\widetilde{\widetilde{H}}(\mathbf{x},\mathbf{y},\mathbf{p}_s,\mathbf{p}_r) \\
&= \Re\{\sum_{\omega}\omega^4|f_s(\omega)|^2A_s^2(\omega)A_r^2(\omega) \\
&\times\sum_{\mathbf{x}_s}w_s(\mathbf{x}_s)G(\mathbf{x},\mathbf{x}_s,\omega)\mathrm{e}^{i\omega\mathbf{p}_s\cdot\mathbf{x}_s} \\
&\times\sum_{\mathbf{x}'_s}w_s(\mathbf{x}'_s)G^*(\mathbf{y},\mathbf{x}'_s,\omega)\mathrm{e}^{-i\omega\mathbf{p}_s\cdot\mathbf{x}'_s} \\
&\times\sum_{\mathbf{x}_r}w_r(\mathbf{x}_r)G(\mathbf{x},\mathbf{x}_r,\omega)\mathrm{e}^{i\omega\mathbf{p}_r\cdot\mathbf{x}_r} \\
&\times\sum_{\mathbf{x}'_r}w_r(\mathbf{x}'_r)G^*(\mathbf{y},\mathbf{x}'_r,\omega)\mathrm{e}^{-i\omega\mathbf{p}_r\cdot\mathbf{x}'_r}\}. \qquad \text{(B-1)}
\end{aligned}
$$

Integrating over $\mathbf{p}_s=(p_{s_x},p_{s_y})$ and $\mathbf{p}_r=(p_{r_x},p_{r_y})$, and changing the order of summation and integration, we get

$$
\begin{aligned}
&\widetilde{\widetilde{H}}(\mathbf{x},\mathbf{y})=\int_{-\infty}^{+\infty}\int_{-\infty}^{+\infty}\widetilde{\widetilde{H}}(\mathbf{x},\mathbf{y},\mathbf{p}_s,\mathbf{p}_r)d\mathbf{p}_sd\mathbf{p}_r \\
&= \Re\{\sum_{\omega}\omega^4|f_s(\omega)|^2A_s^2(\omega)A_r^2(\omega) \\
&\times\sum_{\mathbf{x}_s}w_s(\mathbf{x}_s)G(\mathbf{x},\mathbf{x}_s,\omega)\sum_{\mathbf{x}'_s}w_s(\mathbf{x}'_s)G^*(\mathbf{y},\mathbf{x}'_s,\omega) \\
&\times\int_{-\infty}^{+\infty}\mathrm{e}^{-i\omega\mathbf{p}_s\cdot(\mathbf{x}'_s-\mathbf{x}_s)}d\mathbf{p}_s \\
&\times\sum_{\mathbf{x}_r}w_r(\mathbf{x}_r)G(\mathbf{x},\mathbf{x}_r,\omega)\sum_{\mathbf{x}'_r}w_r(\mathbf{x}'_r)G^*(\mathbf{y},\mathbf{x}'_r,\omega) \\
&\times\int_{-\infty}^{+\infty}\mathrm{e}^{-i\omega\mathbf{p}_r\cdot(\mathbf{x}'_r-\mathbf{x}_r)}d\mathbf{p}_r\}. \qquad \text{(B-2)}
\end{aligned}
$$

Once again note that

$$
\begin{aligned}
\int_{-\infty}^{+\infty}\mathrm{e}^{-i\omega\mathbf{p}_s\cdot(\mathbf{x}'_s-\mathbf{x}_s)}d\mathbf{p}_s &= \frac{1}{|\omega|}\delta(\mathbf{x}'_s-\mathbf{x}_s), \qquad \text{(B-3)}\\
\int_{-\infty}^{+\infty}\mathrm{e}^{-i\omega\mathbf{p}_r\cdot(\mathbf{x}'_r-\mathbf{x}_r)}d\mathbf{p}_r &= \frac{1}{|\omega|}\delta(\mathbf{x}'_r-\mathbf{x}_r), \qquad \text{(B-4)}
\end{aligned}
$$

in 2-D and

$$
\begin{aligned}
\int_{-\infty}^{+\infty}\mathrm{e}^{-i\omega\mathbf{p}_s\cdot(\mathbf{x}'_s-\mathbf{x}_s)}d\mathbf{p}_s &= \frac{1}{|\omega|^2}\delta(\mathbf{x}'_s-\mathbf{x}_s), \qquad \text{(B-5)}\\
\int_{-\infty}^{+\infty}\mathrm{e}^{-i\omega\mathbf{p}_r\cdot(\mathbf{x}'_r-\mathbf{x}_r)}d\mathbf{p}_r &= \frac{1}{|\omega|^2}\delta(\mathbf{x}'_r-\mathbf{x}_r), \qquad \text{(B-6)}
\end{aligned}
$$

in 3-D. Thus, if we choose real functions $A_s(\omega)$ and $A_r(\omega)$ satisfying $A_s^2(\omega) = |\omega|$, $A_r^2(\omega) = |\omega|$ in 2-D and $A_s^2(\omega) = |\omega|^2$, $A_r^2(\omega) = |\omega|^2$ in 3-D, then we have

$$\widetilde{\widetilde{H}}(\mathbf{x}, \mathbf{y}) = H(\mathbf{x}, \mathbf{y}). \tag{B-7}$$

REFERENCES

Albertin, U., D. Yingst, P. Kitchenside, and V. Tcheverda, 2004, True-amplitude beam migration: SEG Technical Program Expanded Abstracts, **23**, 949-952.

Beylkin, G., 1985, Imaging of discontinuities in the inverse scattering problem by inversion of a causal generalized Radon transform: Journal of Mathematical Physics, **26**, 99-108.

Biondi, B., 2002, Stable wide-angle Fourier finite-difference downward extrapolation of 3-D wavefields: Geophysics, **67**, 872-882.

Chavent, G. and R.-E. Plessix, 1999, An optimal true-amplitude least-squares prestack depth-migration operator: Geophysics, **64**, 508-515.

Claerbout, J. F., 1971, Towards a unified theory of reflector mapping: Geophysics, **36**, 467-481.

Claerbout, J. F., 1985, Imaging the earths interior: Blackwell Scientific Publication.

Clapp, M. L., 2005, Imaging Under Salt: Illumination Compensation by Regularized Inversion: PhD thesis, Stanford University.

Etgen, J. T., 2005, How many angles do we really need for delayed-shot migration?: SEG Technical Program Expanded Abstracts, **24**, 1985–1988.

Gelius, L.-J., I. Lecomte, and H. Tabti, 2002, Analysis of the resolution function in seismic prestack imaging: Geophysical Prospecting, **50**, 505–515.

Guitton, A., 2004, Amplitude and kinematic corrections of migrated images for nonunitary imaging operators: Geophysics, **69**, 1017-1024.

Hoffmann, J., 2001, Illumination, resolution, and image quality of PP- and PS-waves for survey planning: The Leading Edge, **20**, 1008–1014.

Kuhl, H. and M. D. Sacchi, 2003, Least-squares wave-equation migration for AVP/AVA inversion: Geophysics, **68**, 262-273.

Lailly, P., 1983, The seismic inverse problem as a sequence of before stack migration: Proc. Conf. on Inverse Scattering, Theory and Applications, Expanded Abstracts, Philadelphia, SIAM.

Lecomte, I., 2008, Resolution and illumination analyses in PSDM: A ray-based approach: The Leading Edge, **27**, no. 5, 650–663.

Lecomte, I. and L.-J. Gelius, 1998, Have a look at the resolution of prestack depth migration for any model, survey and wavefields: SEG Technical Program Expanded Abstracts, **17**, 1112-1115.

Liu, F., D. W. Hanson, N. D. Whitmore, R. S. Day, and R. H. Stolt, 2006, Toward a unified analysis for source plane-wave migration: Geophysics, **71**, no. 4, S129-S139.

Nemeth, T., C. Wu, and G. Schuster, 1999, Least-squares migration of incomplete reflection data: Geophysics, **64**, 208-221.

Paffenholz, J., J. Stefani, B. McLain, and K. Bishop, 2002, SIGSBEE 2A Synthetic subsalt dataset - Image quality as function of migration algorithm and velocity model error: 64th Annual International Meeting, European Association of Geoscience Engineers, Extended Abstracts, B019.

Plessix, R.-E. and W. A. Mulder, 2004, Frequency-domain finite-difference amplitude-preserving migration: Geophysical Journal International, **157**, 975-987.

Pratt, R. G., C. Shin, and G. J. Hicks, 1998, Gauss-Newton and full Newton methods in frequency-space seismic waveform inversion: Geophysical Journal International, **133**, 341-362.

Prucha, M. L. and B. L. Biondi, 2002, Subsalt event regularization with steering filters: SEG Technical Program Expanded Abstracts, **21**, 1176–1179.

Rickett, J. E., 2003, Illumination-based normalization for wave-equation depth migration:

Geophysics, **68**, 1371-1379.

Ristow, D. and T. Rühl, 1994, Fourier finite-difference migration: Geophysics, **59**, 1882-1893.

Romero, L. A., D. C. Ghiglia, C. C. Ober, and S. A. Morton, 2000, Phase encoding of shot records in prestack migration: Geophysics, **65**, 426-436.

Sjoeberg, T. A., L.-J. Gelius, and I. Lecomte, 2003, 2-D deconvolution of seismic image blur: SEG Technical Program Expanded Abstracts, **22**, 1055-1058.

Stoffa, P. L., J. T. Fokkema, R. M. de Luna Freire, and W. P. Kessinger, 1990, Split-step Fourier migration: Geophysics, **55**, 410-421.

Stolt, R. H. and A. Benson, 1986, Seismic Migration: Theory and Practice: Geophysical Press.

Stork, C. and J. Kapoor, 2004, How many P values do you want to migrate for delayed shot wave equation migration?: SEG Technical Program Expanded Abstracts, **23**, 1041-1044.

———, 2006, On "Delayed-shot 3D depth migration": Geophysics, **71**, no. 5, X25-X27.

Symes, W. W., 2008, Approximate linearized inversion by optimal scaling of prestack depth migration: Geophysics, **73**, no. 2, R23–R35.

Tarantola, A., 1984, Inversion of seismic reflection data in the acoustic approximation: Geophysics, **49**, 1259–1266.

Tarantola, 1987, Inverse problem theory: Methods for data fitting and model parameter estimation: Elsevier.

Valenciano, A., 2008, Imaging by Wave-equation Inversion: PhD thesis, Stanford University.

Valenciano, A. A., B. Biondi, and A. Guitton, 2006, Target-oriented wave-equation inversion: Geophysics, **71**, no. 4, A35-A38.

Whitmore, N. D., 1995, An Imaging Hierarchy for Common Angle Plane Wave Seismogram:

PhD thesis, University of Tulsa.

Xie, X.-B., S. Jin, and R.-S. Wu, 2006, Wave-equation-based seismic illumination analysis: Geophysics, **71**, no. 5, S169-S177.

Yu, J., J. Hu, G. T. Schuster, and R. Estill, 2006, Prestack migration deconvolution: Geophysics, **71**, no. 2, S53–S62.

Zhang, Y., J. Sun, C. Notfors, S. H. Gray, L. Chernis, and J. Young, 2005, Delayed-shot 3D depth migration: Geophysics, **70**, no. 5, E21-E28.

———, 2006, Reply to the discussion: Geophysics, **71**, no. 5, X27–X29.

LIST OF TABLES

LIST OF FIGURES

realization.

6 The local Hessian operator for image point at $x = 0.5$ km and $z = 1.5$ km. (a) The exact diagonal of the Hessian; (b) the receiver-side randomly phase encoded Hessian with only one random realization.

7 Sigsbee2A stratigraphic velocity model.

8 Diagonal of the Hessian for the Sigsbee2A model. The Hessian is obtained by using receiver-side random-phase encoding, which takes the limited receiver array into consideration. The result shows the Hessian for a frequency band from 5 Hz to 35 Hz.

9 Source-wavefield intensity for the Sigsbee2A model, which assumes the receiver-side Green's functions to be constant; it ignores the effects of the limited receiver aperture and over-estimates the total energy that enters the earth and returns to be recorded by the receivers.

10 Conventional one-way wave-equation shot-profile migration result of the Sigsbee2A model. Note the uneven illumination below the salt.

11 The migrated image (Figure 10) is normalized by the diagonal of the Hessian shown in Figure 8.

12 The migrated image (Figure 10) is normalized by the source-wavefield intensity shown in Figure 9.

13 Receiver-side randomly phase-encoded Hessian operators for the Sigsbee2A model. Panel (a) shows the diagonal part for a particular region of interest under the salt. Note the uneven illumination due the complex salt body and limited acquisition geometry. Panel (b) shows the result obtained by convolving the Hessian operator (with a size 21×21) with a collection of point scatterers. Note the non-stationarities of the operators.

14 Comparison between migration and inversion. Panel (a) shows the migrated result

(b) shows the inversion result using the receiver-side randomly phase-encoded Hessian operator and (c) is the filtered true reflectivity. All three panels are plotted with the same scale.

15 Normalized residual vs. number of iterations for the Sigsbee2A model; the inversion converges after about 12 iterations.

16 A closeup view of (a) the migrated image, (b) the inverted image and (c) the filtered true reflectivity model.

17 The amplitude spectrum of (a) the migrated image (Figure 16a) and (b) the inverted image (Figure 16b). Note the inverted image contains a broader range of spatial frequencies.

18 A horizontal trace at depth 5.1892 km extracted from images shown in Figure 16. The dotted line, solid line and dashed line represent traces extracted from the true reflectivity model, the migrated image and the inverted image, respectively.

LIST OF TABLES

LIST OF FIGURES

realization.

6 The local Hessian operator for image point at $x = 0.5$ km and $z = 1.5$ km. (a) The exact diagonal of the Hessian; (b) the receiver-side randomly phase encoded Hessian with only one random realization.

7 Sigsbee2A stratigraphic velocity model.

8 Diagonal of the Hessian for the Sigsbee2A model. The Hessian is obtained by using receiver-side random-phase encoding, which takes the limited receiver array into consideration. The result shows the Hessian for a frequency band from 5 Hz to 35 Hz.

9 Source-wavefield intensity for the Sigsbee2A model, which assumes the receiver-side Green's functions to be constant; it ignores the effects of the limited receiver aperture and over-estimates the total energy that enters the earth and returns to be recorded by the receivers.

10 Conventional one-way wave-equation shot-profile migration result of the Sigsbee2A model. Note the uneven illumination below the salt.

11 The migrated image (Figure 10) is normalized by the diagonal of the Hessian shown in Figure 8.

12 The migrated image (Figure 10) is normalized by the source-wavefield intensity shown in Figure 9.

13 Receiver-side randomly phase-encoded Hessian operators for the Sigsbee2A model. Panel (a) shows the diagonal part for a particular region of interest under the salt. Note the uneven illumination due the complex salt body and limited acquisition geometry. Panel (b) shows the result obtained by convolving the Hessian operator (with a size 21×21) with a collection of point scatterers. Note the non-stationarities of the operators.

14 Comparison between migration and inversion. Panel (a) shows the migrated result

(b) shows the inversion result using the receiver-side randomly phase-encoded Hessian operator and (c) is the filtered true reflectivity. All three panels are plotted with the same scale.

15 Normalized residual vs. number of iterations for the Sigsbee2A model; the inversion converges after about 12 iterations.

16 A closeup view of (a) the migrated image, (b) the inverted image and (c) the filtered true reflectivity model.

17 The amplitude spectrum of (a) the migrated image (Figure 16a) and (b) the inverted image (Figure 16b). Note the inverted image contains a broader range of spatial frequencies.

18 A horizontal trace at depth 5.1892 km extracted from images shown in Figure 16. The dotted line, solid line and dashed line represent traces extracted from the true reflectivity model, the migrated image and the inverted image, respectively.

Method	Number of wavefield propagations	Number of Greeen's functions to store
Direct computation	$N_x N_y N_\omega$	$M_x M_y M_z N_x N_y N_\omega$
Plane-wave, receiver-side	$(1 + N_{p_{r_x}} N_{p_{r_y}}) N_s N_\omega$	0
Random, receiver-side	$(1 + N_{\text{realize}}) N_s N_\omega$	0

Table 1: Cost comparison for a marine acquisition geometry.

Method	Number of wavefield propagations	Number of Green's functions to store
Direct computation	$N_x N_y N_\omega$	$M_x M_y M_z N_x N_y N_\omega$
Plane-wave, receiver-side	$(1 + N_{p_{r_x}} N_{p_{r_y}}) N_s N_\omega$	0
Plane-wave, simultaneous	$N_{p_{s_x}} N_{p_{s_y}} N_{p_{r_x}} N_{p_{r_y}} N_\omega$	0
Random, receiver-side	$(1 + N_{\text{realize}}) N_s N_\omega$	0
Random, simultaneous	$2 N_{\text{realize}} N_\omega$	0

Table 2: Cost comparison for an OBS or a land acquisition geometry.

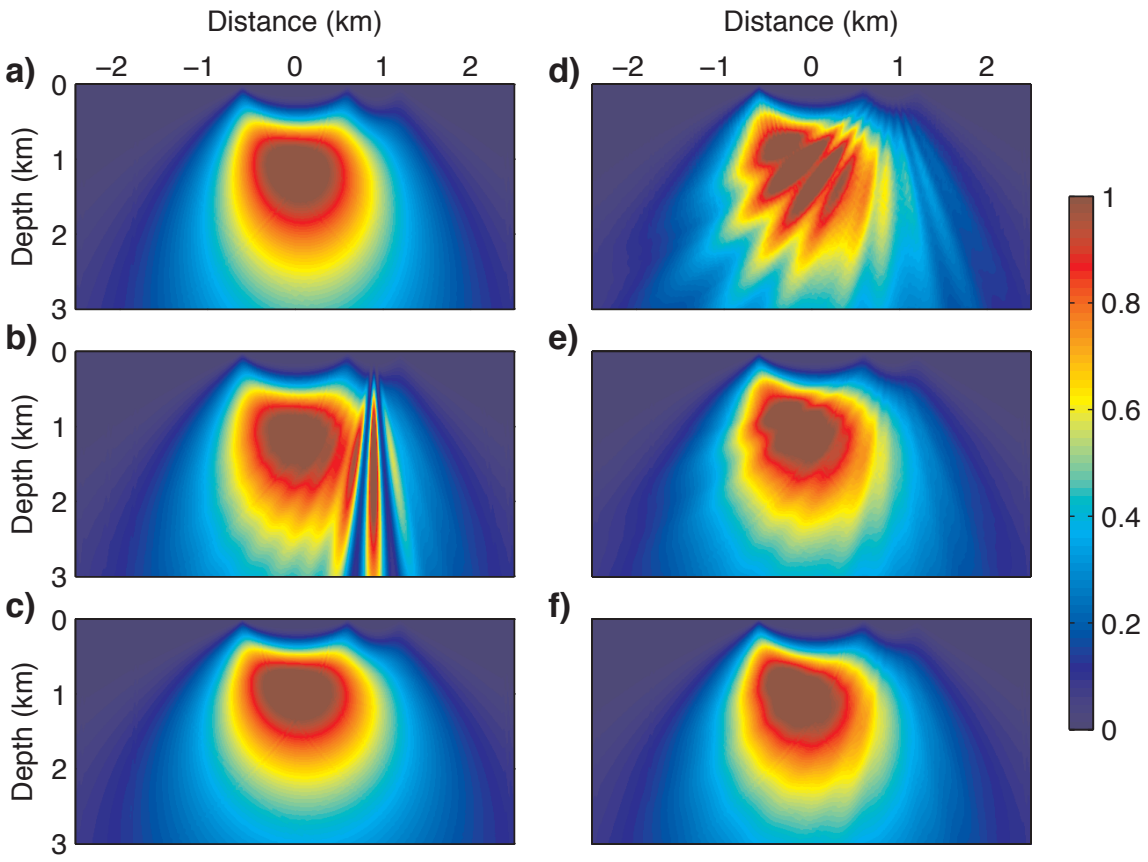

Figure 1: Diagonal of the Hessian for a constant-velocity model with one shot and two receivers. (a) The exact diagonal of the Hessian (equation 7); (b) the Hessian contaminated by crosstalk (equation 8 with $\alpha(\mathbf{x}_r, \mathbf{p}_r, \omega) = 1$); (c) the receiver-side plane-wave phase-encoded Hessian; (d), (e) and (f) are the receiver-side randomly phase-encoded Hessians obtained with 1, 5 and 20 random realizations, respectively.

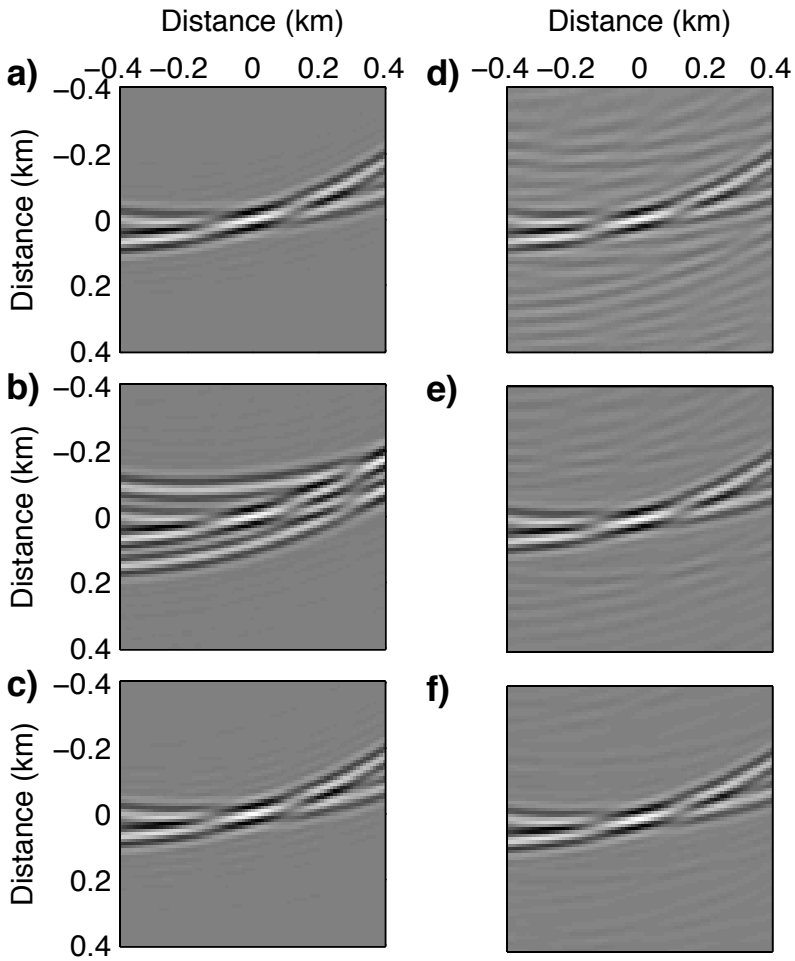

Figure 2: The local Hessian operator for image point $x = 0.5$ km, $z = 1.5$ km (a row of the Hessian matrix). The acquisition geometry is the same as that in Figure 1. The size of the Hessian operator is 81 samples in both x and z directions. (a) The exact Hessian; (b) The Hessian contaminated by crosstalk; (c) the receiver-side plane-wave phase-encoded Hessian; (d), (e) and (f) are the receiver-side randomly phase-encoded Hessian obtained with 1, 5 and 20 random realizations, respectively.

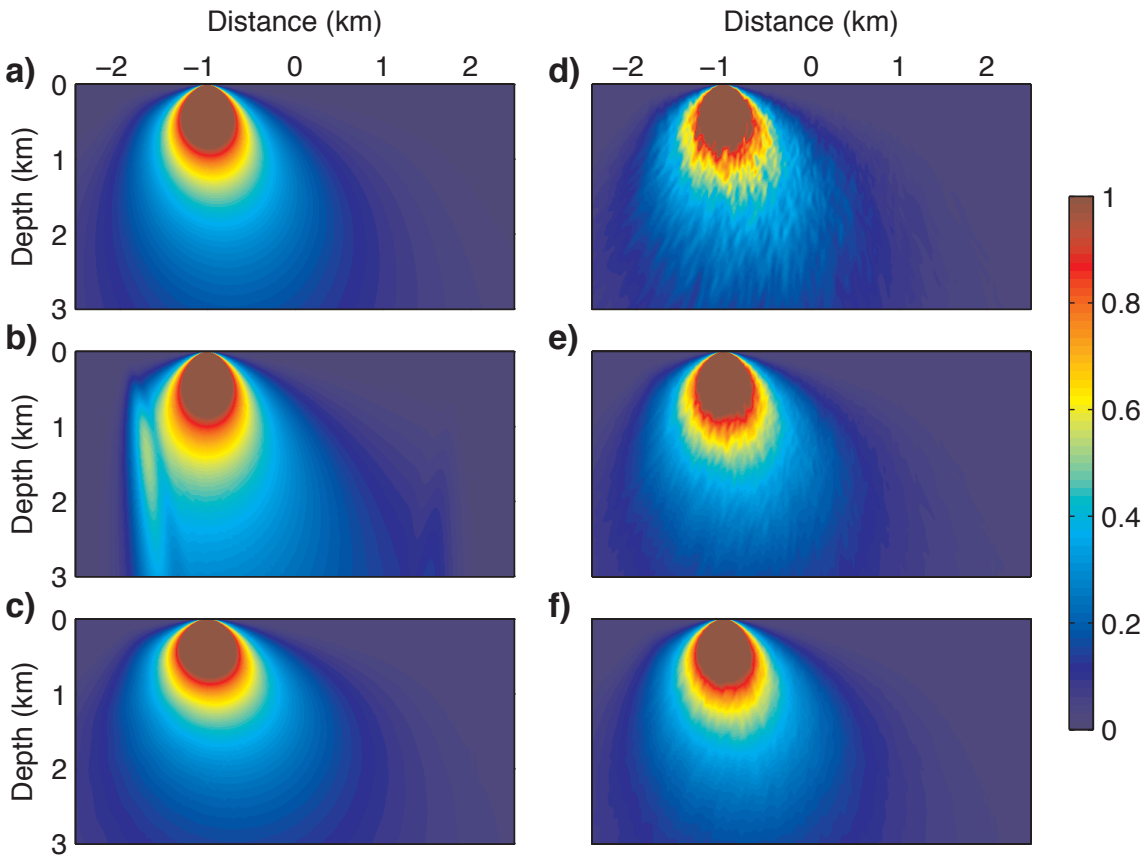

Figure 3: Diagonal of the Hessian for a constant-velocity model with one shot and 401 receivers. (a) The exact diagonal of the Hessian; (b) the Hessian contaminated by crosstalk; (c) the receiver-side plane-wave phase-encoded Hessian; (d), (e) and (f) are the receiver-side randomly phase-encoded Hessians obtained with 1, 5 and 20 random realizations, respectively.

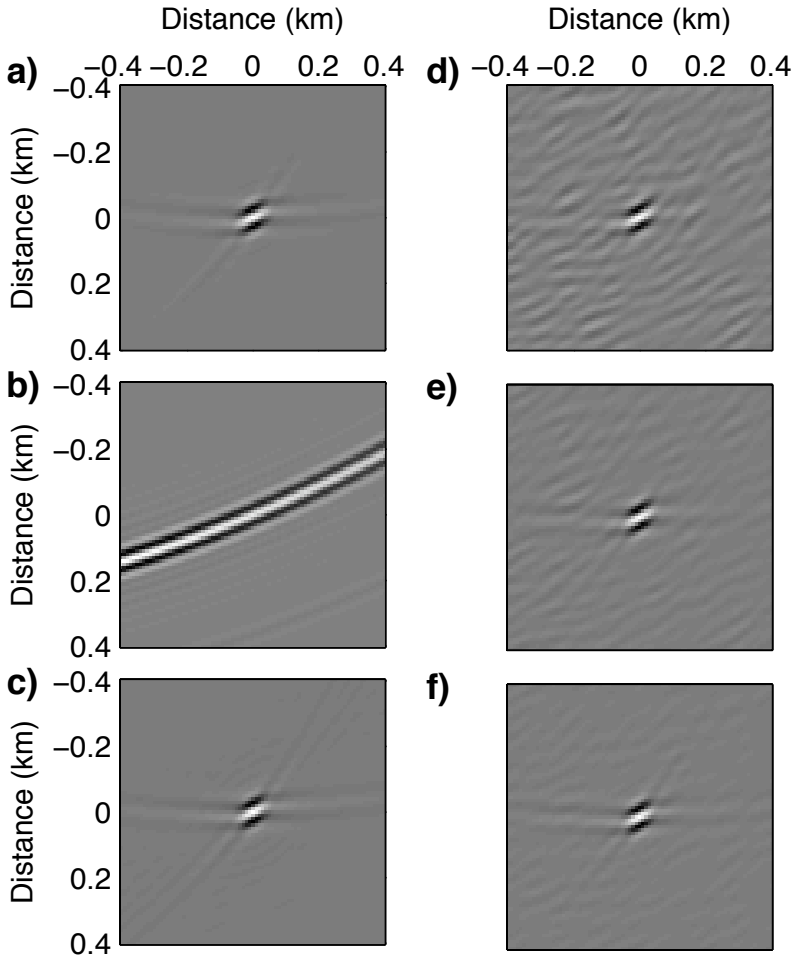

Figure 4: The local Hessian operator for image point $x = 0.5$ km, $z = 1.5$ km. The acquisition geometry is the same as that in Figure 3. (a) The exact Hessian; (b) The Hessian contaminated by crosstalk; (c) the receiver-side plane-wave phase-encoded Hessian; (d), (e) and (f) are the receiver-side randomly phase-encoded Hessian obtained with 1, 5 and 20 random realizations, respectively.

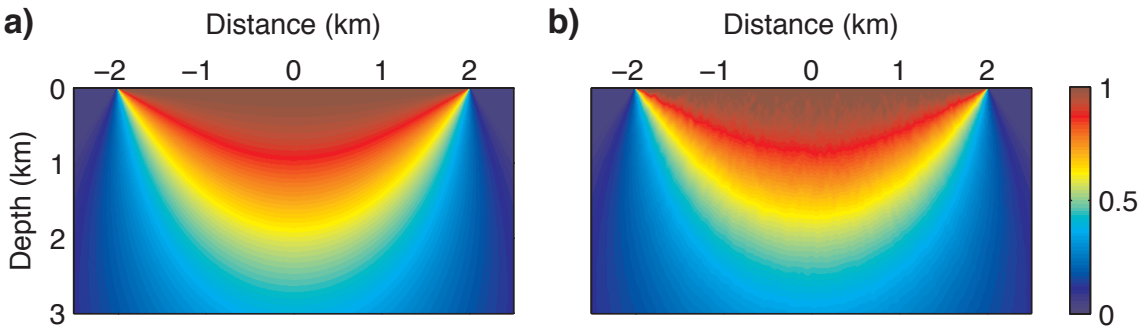

Figure 5: Diagonal of the Hessian with 401 shots and 401 receivers. (a) The exact diagonal of the Hessian; (b) the receiver-side randomly phase encoded Hessian with only one random realization.

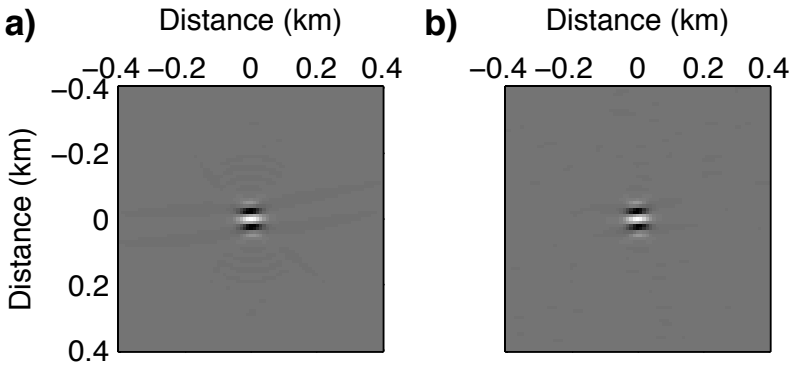

Figure 6: The local Hessian operator for image point at $x = 0.5$ km and $z = 1.5$ km. (a) The exact diagonal of the Hessian; (b) the receiver-side randomly phase encoded Hessian with only one random realization.

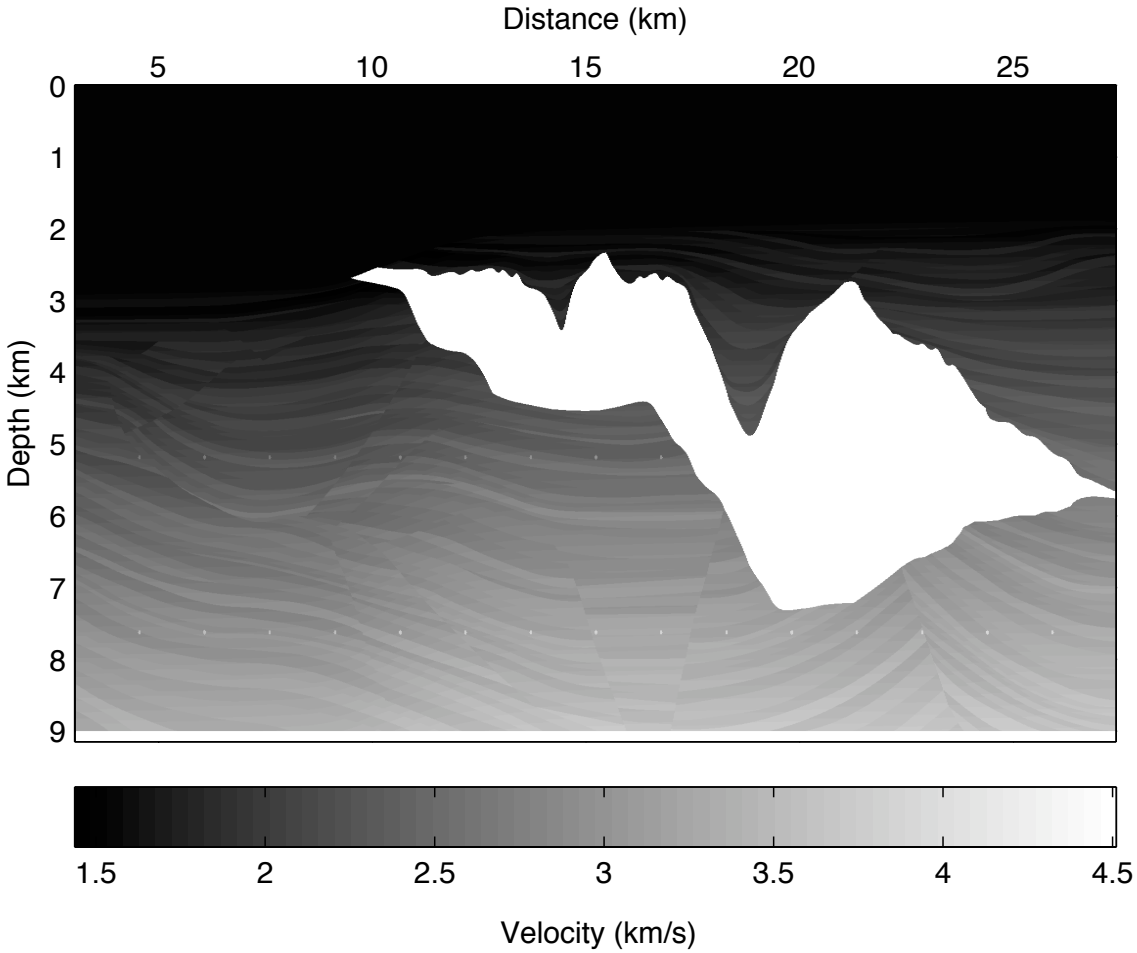

Figure 7: Sigsbee2A stratigraphic velocity model.**Tang – GEO-2008-0443**

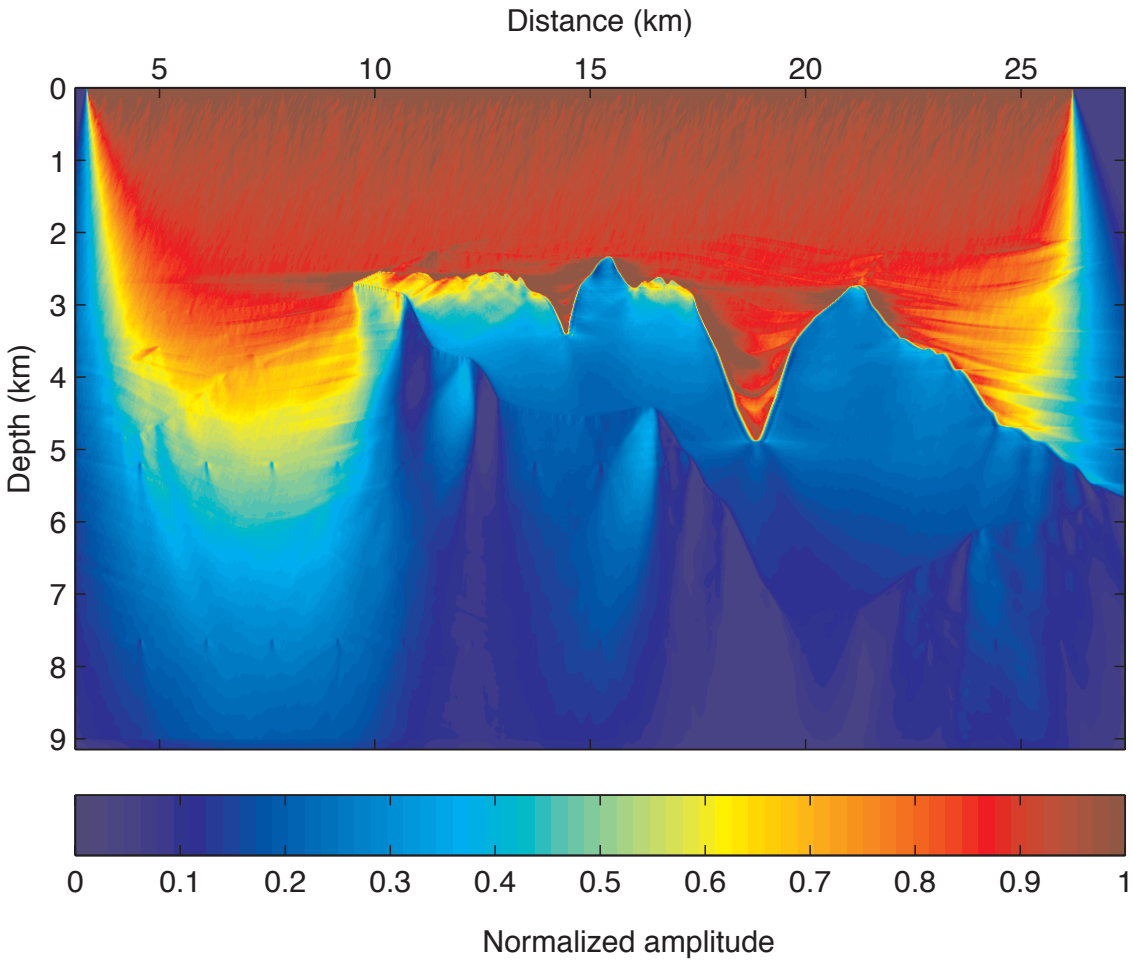

Figure 8: Diagonal of the Hessian for the Sigsbee2A model. The Hessian is obtained by using receiver-side random-phase encoding, which takes the limited receiver array into consideration. The result shows the Hessian for a frequency band from 5 Hz to 35 Hz.

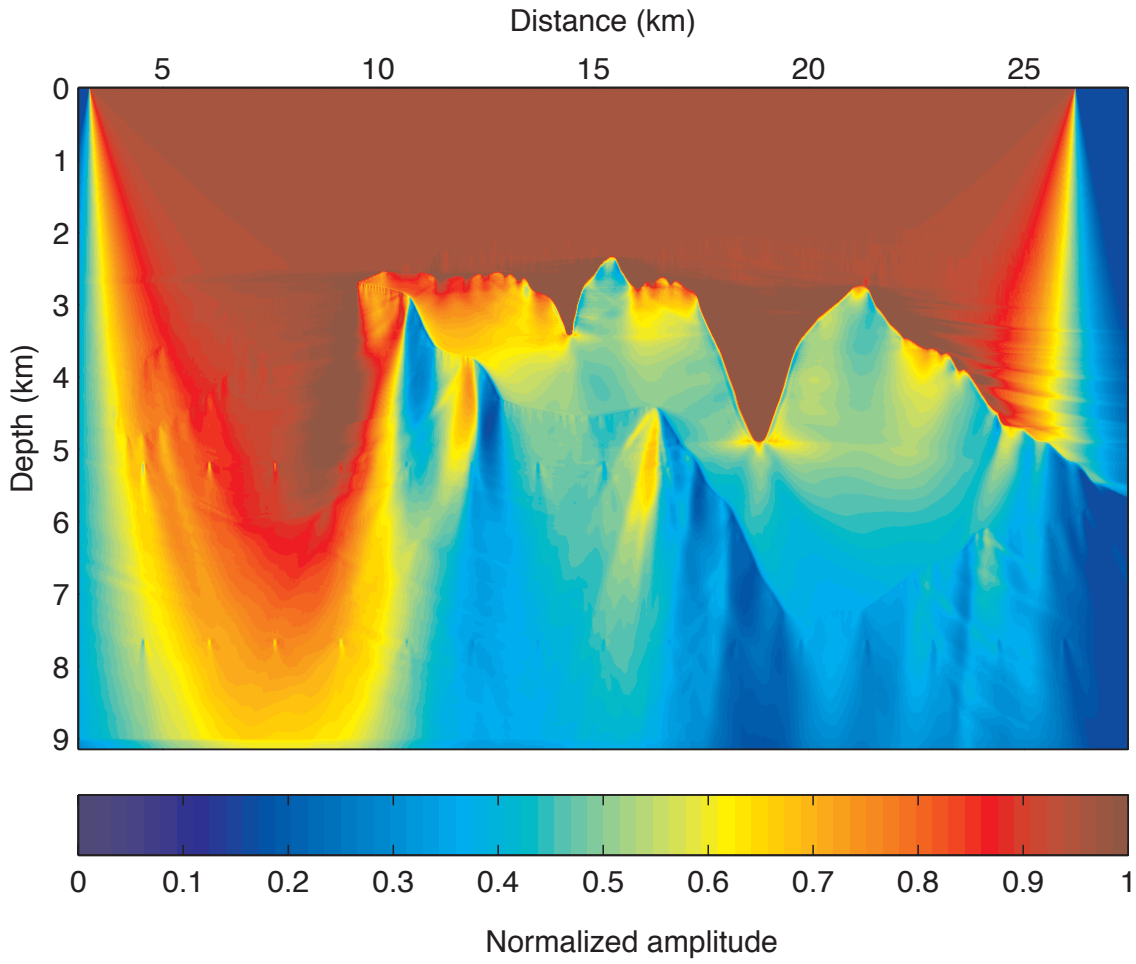

Figure 9: Source-wavefield intensity for the Sigsbee2A model, which assumes the receiver-side Green's functions to be constant; it ignores the effects of the limited receiver aperture and over-estimates the total energy that enters the earth and returns to be recorded by the receivers.

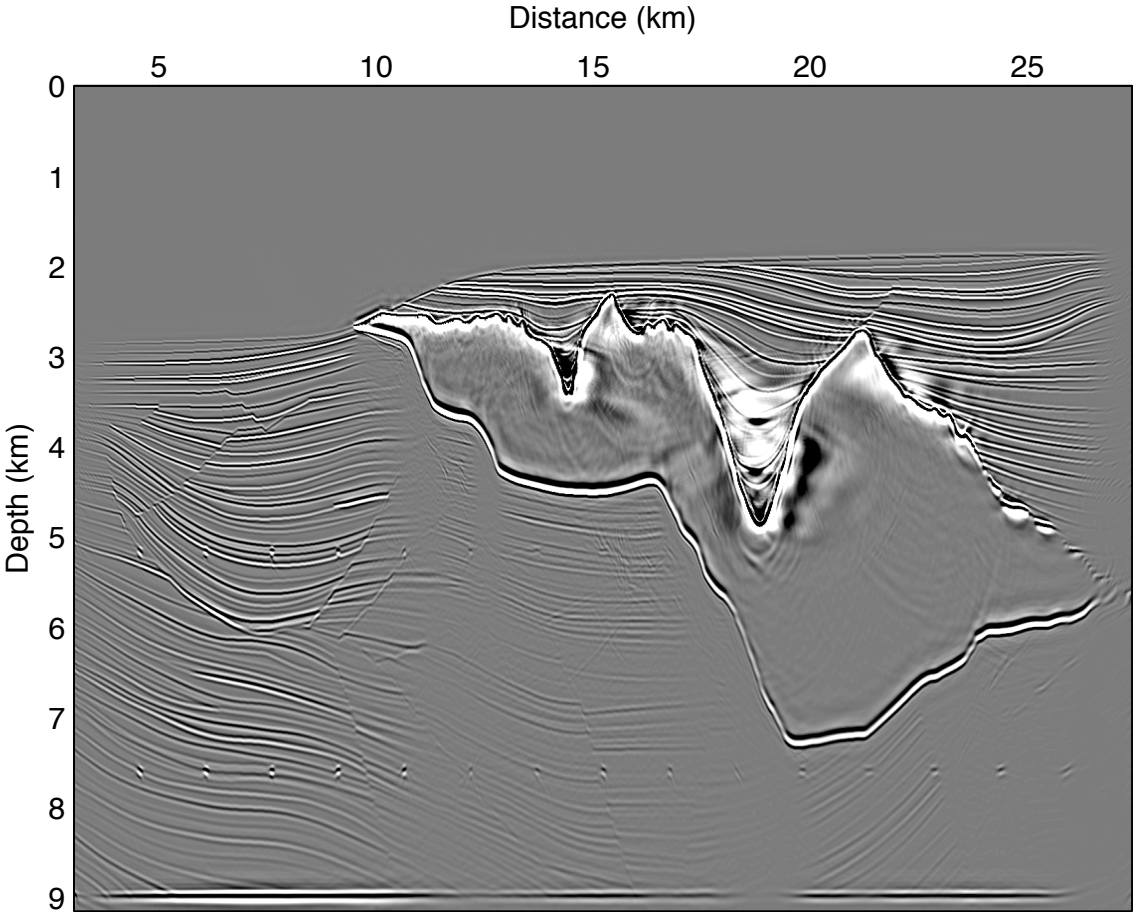

Figure 10: Conventional one-way wave-equation shot-profile migration result of the Sigsbee2A model. Note the uneven illumination below the salt.

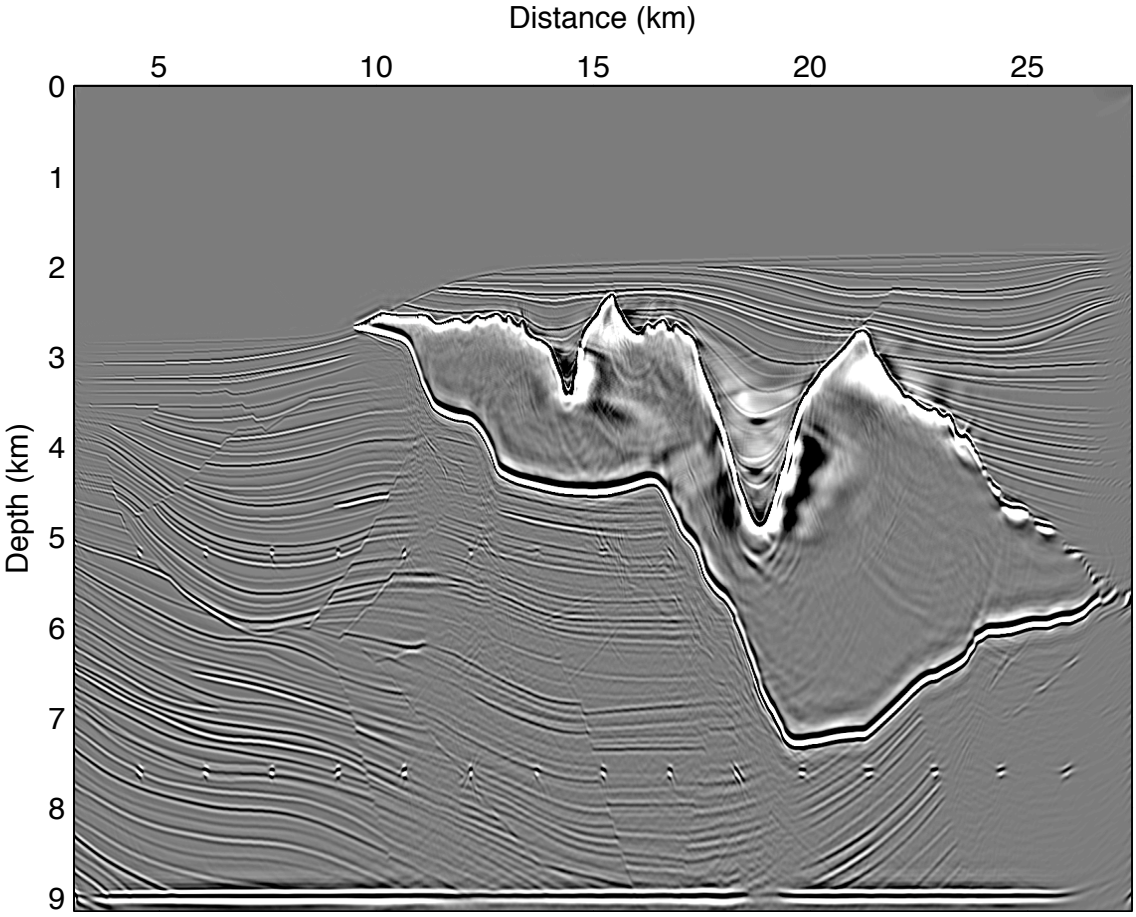

Figure 11: The migrated image (Figure 10) is normalized by the diagonal of the Hessian shown in Figure 8.

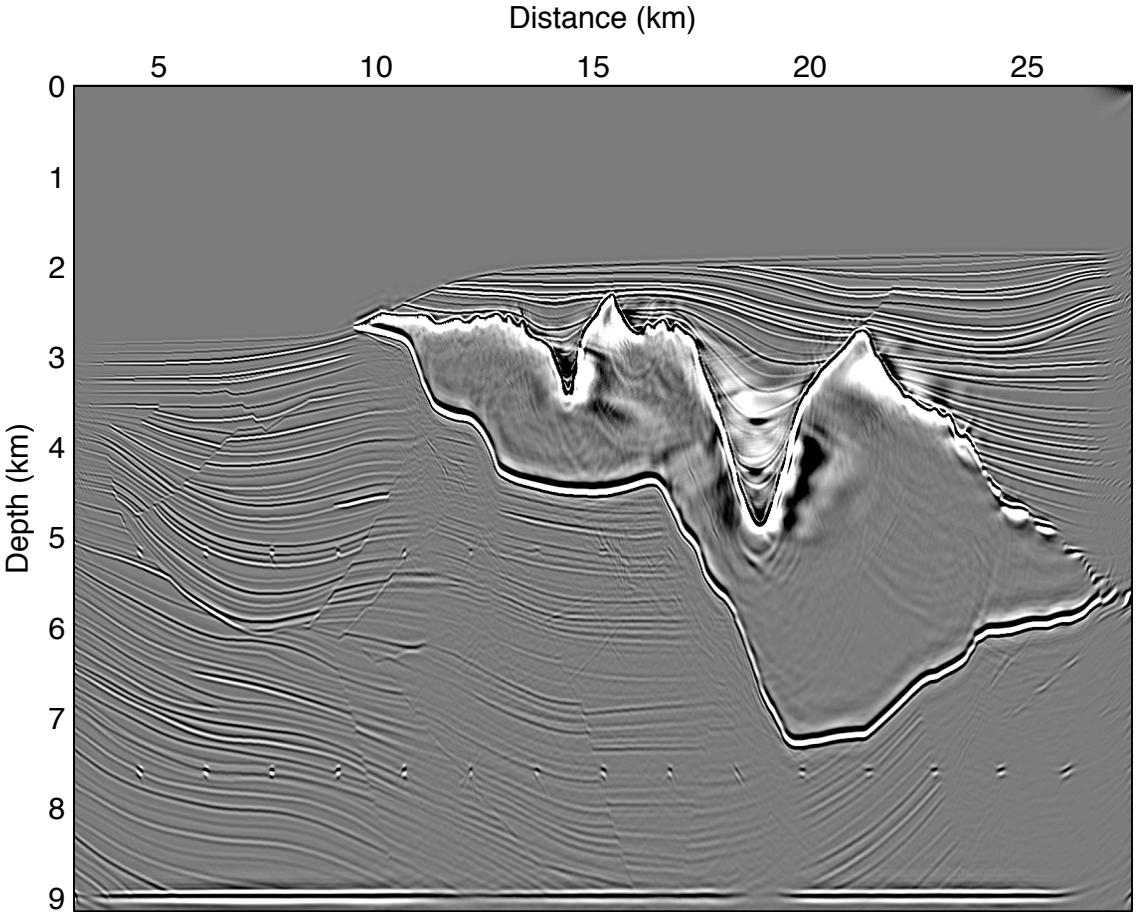

Figure 12: The migrated image (Figure 10) is normalized by the source-wavefield intensity shown in Figure 9.

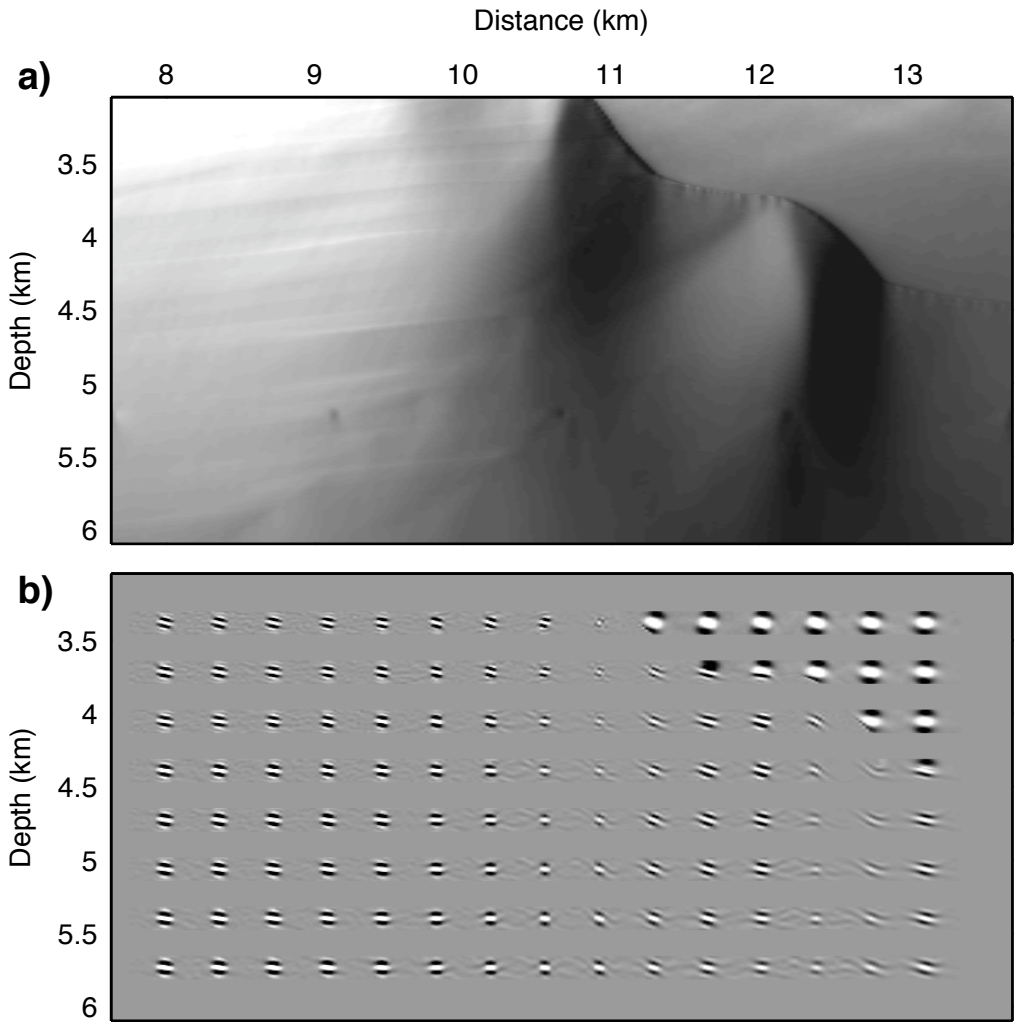

Figure 13: Receiver-side randomly phase-encoded Hessian operators for the Sigsbee2A model. Panel (a) shows the diagonal part for a particular region of interest under the salt. Note the uneven illumination due the complex salt body and limited acquisition geometry. Panel (b) shows the result obtained by convolving the Hessian operator (with a size 21×21) with a collection of point scatterers. Note the non-stationarities of the operators.

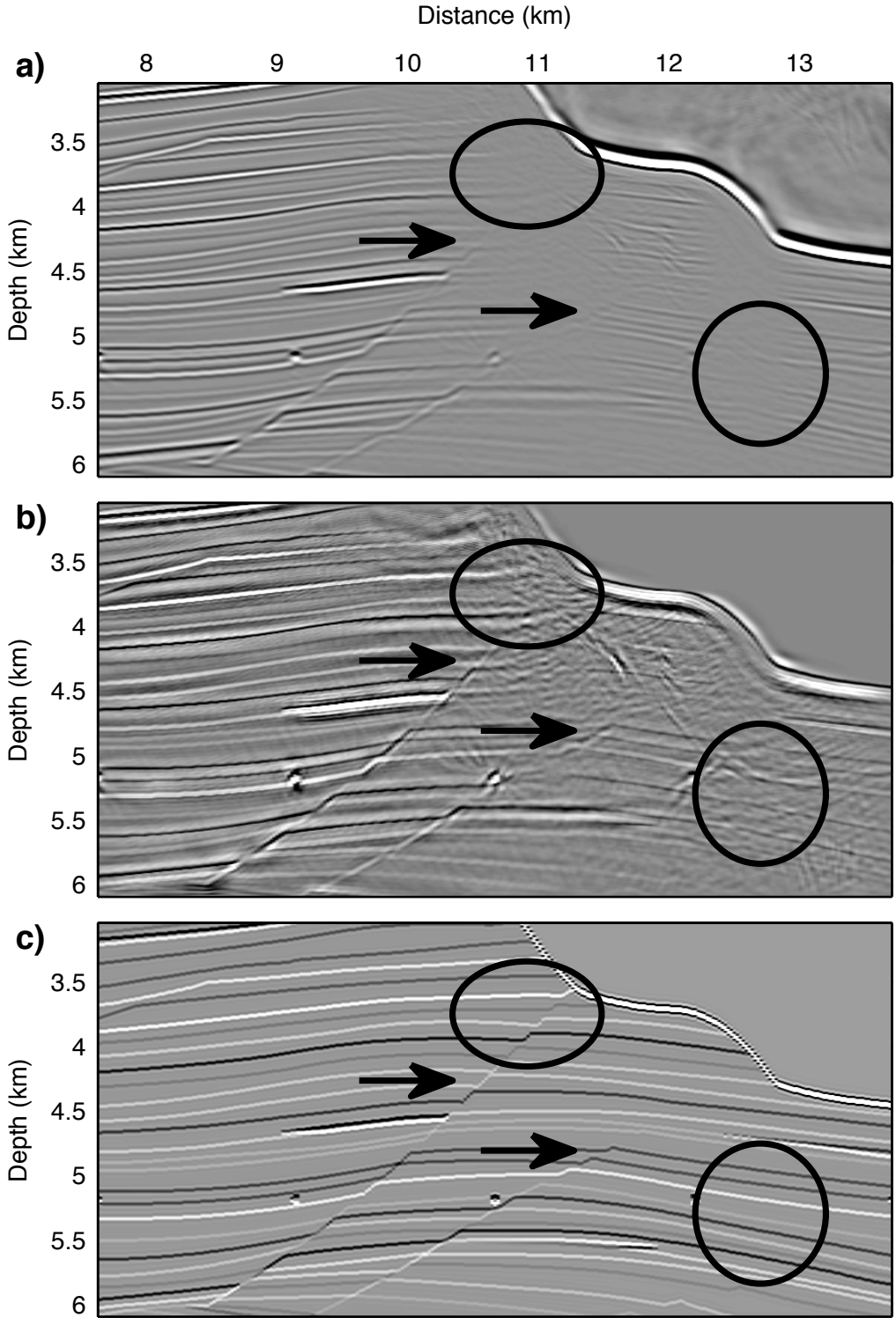

Figure 14: Comparison between migration and inversion. Panel (a) shows the migrated result (b) shows the inversion result using the receiver-side randomly phase-encoded Hessian operator and (c) is the filtered true reflectivity. All three panels are plotted with the same

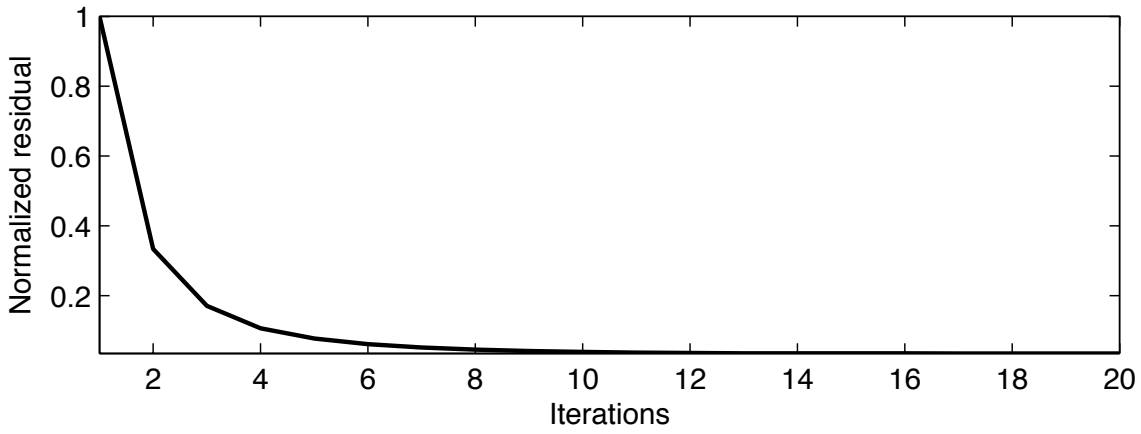

Figure 15: Normalized residual vs. number of iterations for the Sigsbee2A model; the inversion converges after about 12 iterations.

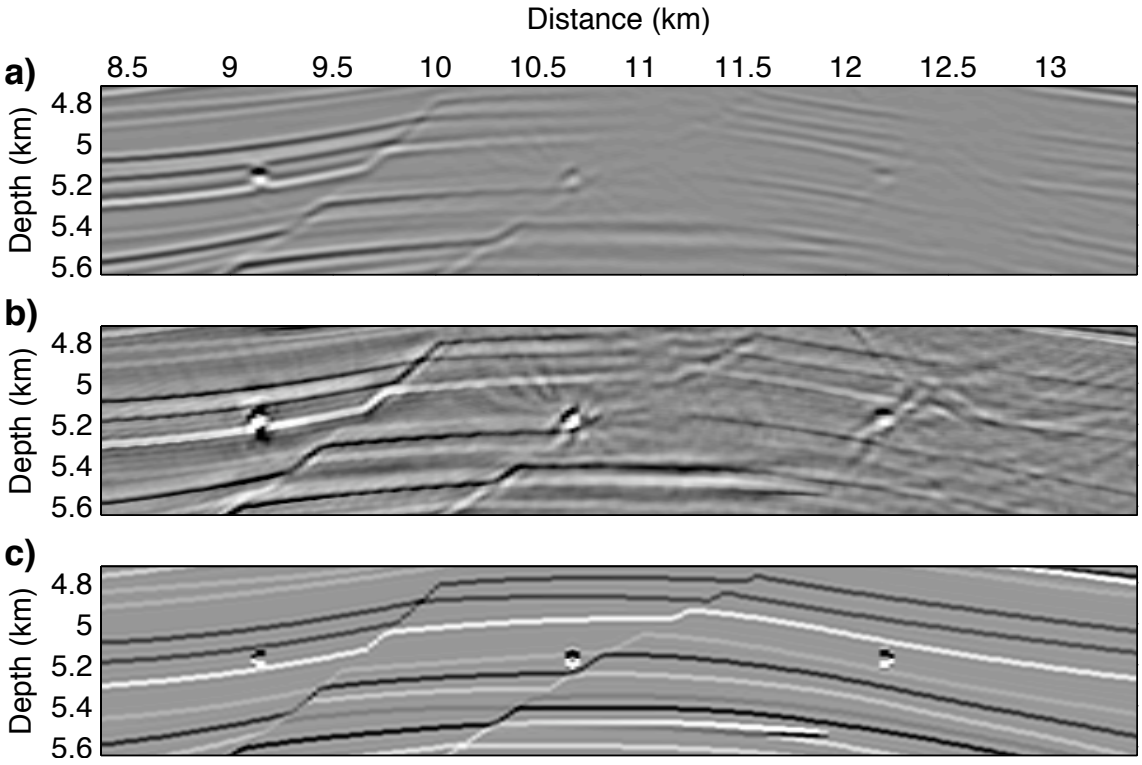

Figure 16: A closeup view of (a) the migrated image, (b) the inverted image and (c) the filtered true reflectivity model.

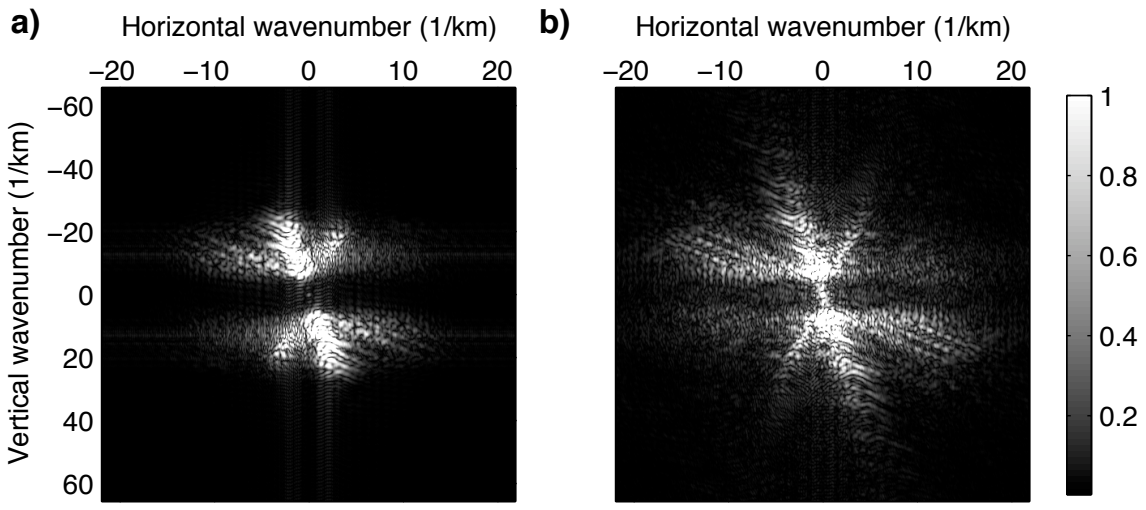

Figure 17: The amplitude spectrum of (a) the migrated image (Figure 16a) and (b) the inverted image (Figure 16b). Note the inverted image contains a broader range of spatial frequencies.

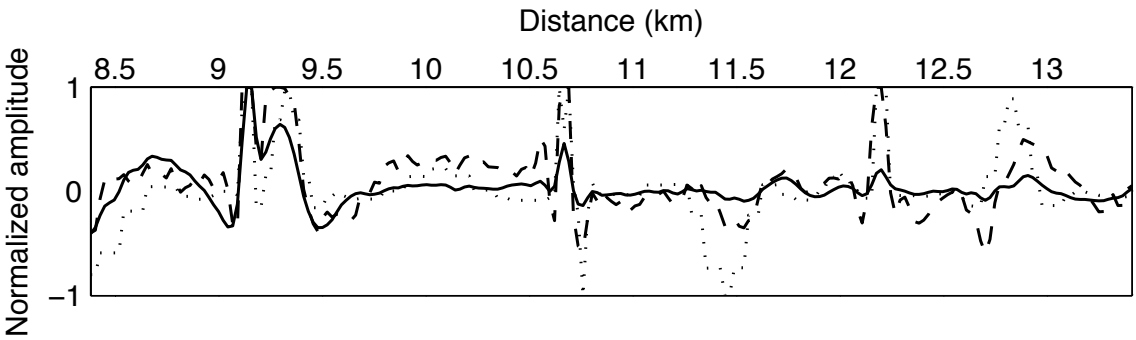

Figure 18: A horizontal trace at depth 5.1892 km extracted from images shown in Figure 16. The dotted line, solid line and dashed line represent traces extracted from the true reflectivity model, the migrated image and the inverted image, respectively.